

University of Louisville

ThinkIR: The University of Louisville's Institutional Repository

Electronic Theses and Dissertations

5-2014

Development of a light-powered microstructure : enhancing thermal actuation with near-infrared absorbent gold nanoparticles.

Thomas Matthew Lucas
University of Louisville

Follow this and additional works at: <https://ir.library.louisville.edu/etd>



Part of the [Electrical and Computer Engineering Commons](#)

Recommended Citation

Lucas, Thomas Matthew, "Development of a light-powered microstructure : enhancing thermal actuation with near-infrared absorbent gold nanoparticles." (2014). *Electronic Theses and Dissertations*. Paper 862. <https://doi.org/10.18297/etd/862>

This Doctoral Dissertation is brought to you for free and open access by ThinkIR: The University of Louisville's Institutional Repository. It has been accepted for inclusion in Electronic Theses and Dissertations by an authorized administrator of ThinkIR: The University of Louisville's Institutional Repository. This title appears here courtesy of the author, who has retained all other copyrights. For more information, please contact thinkir@louisville.edu.

DEVELOPMENT OF A LIGHT-POWERED MICROSTRUCTURE:
ENHANCING THERMAL ACTUATION WITH NEAR-INFRARED
ABSORBENT GOLD NANOPARTICLES

By

Thomas Matthew Lucas

B.S., Electrical and Computer Engineering, University of Louisville, 2009
M.Eng., Electrical and Computer Engineering, University of Louisville, 2010

A Dissertation
Submitted to the Faculty of the
J. B. Speed School of Engineering of the University of Louisville
In Partial Fulfillment of the Requirements
For the Degree of

Doctor of Philosophy

Electrical and Computer Engineering Department
University of Louisville
Louisville, Kentucky

May 2014

Copyright 2014 by Thomas Matthew Lucas

All rights reserved

DEVELOPMENT OF A LIGHT-POWERED MICROSTRUCTURE:
ENHANCING THERMAL ACTUATION WITH NEAR-INFRARED
ABSORBENT GOLD NANOPARTICLES

By

Thomas Matthew Lucas

B.S., Electrical and Computer Engineering, University of Louisville, 2009
M.Eng., Electrical and Computer Engineering, University of Louisville, 2010

A Dissertation Approved on

April 7, 2014

by the following Dissertation Committee

Cindy Harnett, PhD,
Dissertation Director

John Naber, PhD

Shamus McNamara, PhD

Stuart Williams, PhD

Roger Bradshaw, PhD

DEDICATION

To my family, friends, and future.

ACKNOWLEDGEMENTS

I would like to give specific thanks to Damien Wilburn, Tyler Kilgore, and Tyler ‘Tweek’ Adams for a decade of friendship, support, and shenanigans. I also extend my gratitude to Cindy Harnett for her intellectual support and guidance, and Evgeniya Moiseeva for teaching me how to be a graduate student.

ABSTRACT

DEVELOPMENT OF A LIGHT-POWERED MICROSTRUCTURE: ENHANCING THERMAL ACTUATION WITH NEAR-INFRARED ABSORBENT GOLD NANOPARTICLES

Thomas M. Lucas

April 7, 2014

Development of microscale actuating technologies has considerably added to the toolset for interacting with natural components at the cellular level. Small-scale actuators and switches have potential in areas such as microscale pumping and particle manipulation. Thermal actuation has been used with asymmetric geometry to create large deflections with high force relative to electrostatically driven systems. However, many thermally based techniques require a physical connection for power and operate outside the temperature range conducive for biological studies and medical applications. The work presented here describes the design of an out-of-plane bistable switch that responds to near-infrared light with wavelength-specific response.

In contrast to thermal actuating principles that require wired conductive components for Joule heating, the devices shown here are wirelessly powered by near – infrared (IR) light by patterning a wavelength-specific absorbent gold nanoparticle (GNP) film onto the microstructure. An optical window exists which allows near-IR wavelength light to permeate living tissue, and high stress mismatch in the bilayer geometry allows for large actuation at biologically acceptable limits. Patterning the GNP film will allow thermal gradients to be created from a single laser source, and integration of various

target wavelengths will allow for microelectromechanical (MEMS) devices with multiple operating modes. An optically induced temperature gradient using wavelength-selective printable or spinnable coatings would provide a versatile method of wireless and non-invasive thermal actuation. This project aims to provide a fundamental understanding of the particle and surface interaction for bioengineering applications based on a “hybrid” of infrared resonant gold nanoparticles and MEMS structures.

This hybrid technology has potential applications in light-actuated switches and other mechanical structures. Deposition methods and surface chemistry are integrated with three-dimensional MEMS structures in this work. The long-term goal of this project is a system of light-powered microactuators for exploring cells' response to mechanical stimuli, adding to the fundamental understanding of tissue response to everyday mechanical stresses at the molecular level.

TABLE OF CONTENTS

	PAGE
DEDICATION	iii
ACKNOWLEDGEMENTS	iv
ABSTRACT	v
LIST OF FIGURES	xi
CHAPTER	
1. INTRODUCTION	1
1.1. Mechanical Sensing	2
1.1.1. Microfluidic Sensing	5
1.2. Active Microfluidics and Actuators	8
1.2.1. Microfluidic Pumping and Mixing	8
1.2.2. Microactuators	9
1.3. Light-Driven Thermal Actuators	11
1.4. Bistable geometry	13
1.4.1. Buckled Beam Theory	13
1.4.2. Bistable Out-of-Plane Structures	16
1.5. A MEMS – Gold Nanoparticle Hybrid	18
2. MECHANICAL CHARACTERIZATION OF BILAYER STRUCTURES	20
2.1. Bilayer Interaction with Microbubbles	21
2.1.1. Motivation for a Bubble Shield	21

2.1.2. Microbubble and Trap Theory	22
2.1.3. Experimental Methods	24
2.1.4. Analysis of Bilayer-Bubble Interaction	25
2.1.5. Insight into Elastocapillary Length	26
2.2. Bistable Bilayers Subjected to Lift and Drag Forces	29
2.2.1. Windowpane Theory of Bistability	30
2.2.2. Suspended Bilayer Fabrication	32
2.2.3. Method of Applying Flow to a Pop-up Element	34
2.2.4. Discussion of the Force Interaction	35
2.2.5. Applications in Air Flow Sensing	36
2.3. Monitoring a Suspended Element	38
2.3.1. Electronic Sensing	38
2.3.2. Optical Detection	39
2.3.3. Advantages of Autonomous Sensing	41
3. AN OPTIMIZED POLYMER FILM WITH GOLD NANOPARTICLES	42
3.1. Developing a GNP Film	43
3.2. Plasmonic Heating Characterization	45
3.2.1. Particle and Substrate Fabrication	45
3.2.2. Nanoparticle Dispersion	48
3.3. Characterization Objectives	50
3.3.1. Experimental Setup	51
3.4. Particle Effect on Surface Heating	54
3.4.1. Thermal Efficiency	56

3.4.2. Response to Varied Intensity	58
3.5. Conclusions on Single Wavelength Tuned Film	60
4. PARTICLE FILMS AT TWO WAVELENGTHS	61
4.1. Wavelength-Tuned Particles	62
4.1.1. Synthesizing Gold Nanoparticles	63
4.1.2. Film Deposition	65
4.2. Experiment Setup	67
4.3. Interpreting the Surface Performance	69
4.4. Possible Optimizations	73
5. ENHANCING LIGHT-INDUCED THERMAL ACTUATION	74
5.1. Gold Nanoparticles with Pop-up Structures	75
5.2. Fabrication	77
5.2.1. Gold Nanoparticle Synthesis	77
5.2.2. Cleanroom Processing	78
5.3. Experiment Setup	80
5.3.1. Laser Control and Device Monitoring	80
5.3.2. Segmenting the Reflection in the Images	81
5.4. Results	83
5.5. Discussion	85
5.6. Conclusions from this Experiment	86
6. CONCLUSION	87
6.1. Future Directions	88
6.1.1. Complex and Streamlined Fabrication	88

6.1.2. IR Transparent Materials	89
6.2. Conclusions	90
REFERENCES	91
CURRICULUM VITAE	107

LIST OF FIGURES

Figure 1- A typical compressed beam structure. The beam is suspended between two anchors [74].	14
Figure 2 - Characteristic S-Curve associated with bistable compressed beams [74]	15
Figure 3 - SEM view of the bistable windowpane structures, released to one of two states.	16
Figure 4 - Array of 300 micron diameter bubble traps undergoing an electroplating sample collection sequence across the front row.	22
Figure 5 - Released cage devices used for bubble generation and trapping.	23
Figure 6 - Measured bubble volume present over 20 minutes plotted beside the ideal gas law predicted generation at 0.8%.	25
Figure 7 - An air bubble trapped in a microcage in water. The filaments conform to the surface of the bubble over a range of bubble diameters. The outline of the original etch pattern remains on the plane of the substrate, while filaments fold around the bubble.	26
Figure 8 - Schematic view of the bistable windowpane device used in this work. Air flow along the down axis will cause a deflection to the other stable state. The transition is only reversible if the air flow direction is rotated 90 degrees.	30
Figure 9 - Potential energy estimation in the bistable windowpane. Switching occurs at the central peak and stable states are at the two local minima.	31

Figure 10 - Fabrication diagram for the cleanroom process used to fabricate the wind sensing devices.	32
Figure 11- Schematic view of the bistable windowpane device used in this work. Air flow along the down axis will cause a deflection to the other stable state. This is only reversible if the air flow direction is rotated 90 degrees.	33
Figure 12 - Picture of the wind tunnel used for experiments with the wind sensor. The top can be removed to allow the test chip to be changed.	34
Figure 13 - Data relating the side length of the folded windowpane with the air flow speed required to cause a state change.	36
Figure 14 - Physical layout and circuit diagram for capacitance measuring across a released device	38
Figure 15 – Horizontal optical measurement	39
Figure 16 - Concave profile for vertical reflection	40
Figure 17 - This Figure shows an overview of the system being characterized in this work. Particles are coated onto a Pt trace on a glass substrate. Light at a certain wavelength is applied. Absorbed light will provide additional thermal energy to the system.	44
Figure 18 - (a) Optical absorption spectrum of synthesized gold nanoparticles, with a TEM image of particles as background. (b) Fabricated planar resistor used to gather temperature measurements. (c) SEM images of GNPs with PVP polymer matrix after spin-coating on the platinum test surface.	47
Figure 19 - Thermal efficiency measurement setup: a LabVIEW console operates the 808 nm laser, and resistance-induced temperature changes are calculated from voltages measured by an amplifier circuit.	51

Figure 20 - Temperature data is averaged from each sample set. The time constant was calculated from the exponential cool down from 120 to 240 seconds and the decay equation is shown in the Figure.	54
Figure 21 - The box plot of the data demonstrates the difference in optical absorption when nanoparticles are applied to the surface.	55
Figure 22 - The intensity levels correspond linearly to temperature.	58
Figure 23- A concept drawing of a patterned gold nanoparticle film that will show a different response to a particular wavelength. Patterned areas may heat more strongly in response to a specific wavelength of light.	63
Figure 24 - The absorption spectrum of the two batches of GNPs used for this experiment.	64
Figure 25 - Drawing of the test thermometer surface used for this work and a SEM image of a GNP film.	66
Figure 26 - Experimental Setup with Two Laser Sources.	67
Figure 27 - Temperature increase vs. Time for GNP-coated and control surfaces illuminated by A) 808 nm and B) 915 nm laser light. (C) A normalized comparison of the temperature increase of each film type.	71
Figure 28 - Illustration of the system being investigated in this experiment.	76
Figure 29 - Absorbance spectrum of the gold nanoparticles synthesized for this study with a peak at 812 nm.	77
Figure 30 - SEM image of the fabricated devices (a), closer view to show the deposited GNPs (b), and a TEM of the gold nanoparticles (c).	79
Figure 31 - Schematic of the setup used for data collection in this system.	81

Figure 32 - Reflection profiles of a pop-up windowpane at different stages (a, b, c), with increasing temperature from left to right. The RGB components of a reflection image (R, G, and B). The segmented reflection used for a pixel count (d).	82
Figure 33 - Reflectivity averaged data for each sample type.	83
Figure 34 - Fitted curves displaying the correlation between light and deflection of the structure with error bars depicting 95% confidence interval of the fit.	85

CHAPTER I

INTRODUCTION

Development of microscale actuating technologies has produced diverse options for interacting with natural components at the cellular level. Small-scale actuators and switches have potential in areas such as microscale pumping and particle manipulation, and microelectromechanical systems (MEMS) sensors have revolutionized the way data is collected from the environment. Sensing techniques developed at the microscale are often more efficient and sensitive than those at the macroscale [1].

MEMS devices can be classified into categories by function and by the physical phenomena used by the device. In this introduction, MEMS applications are divided into sensing and actuating. Within each group, mechanical and microfluidic based techniques are discussed.

This dissertation will catalogue the development of a light-driven thermal actuation technique for integration with MEMS. It will provide a basis for developing bioengineering applications based on a hybrid of infrared resonant gold nanoparticles and MEMS structures, and to manipulate a MEMS structure with light as a proof of concept. The mechanics of the pop-ups and gold nanoparticles are detailed in the chapters following this introduction to MEMS and microfluidic systems.

1.1 Mechanical Sensing

Mechanical sensing can be used to extract parameters from both mechanical and fluid-based phenomena. An example of a mechanics-based sensor would be an accelerator, gyroscope, or pressure sensor. An accelerometer translates the force from an acceleration of a body into an electrical signal through capacitive or piezoresistive elements. A mass element is typically suspended and subject to the same movements as a body that it is attached to [2-4].

A gyroscope is a kind of device based on the principles of angular momentum for measuring or maintaining orientation. Most of the MEMS gyroscopes are based on the Coriolis effect which is an apparent deflection of moving objects when they are viewed from a rotating reference frame. In a reference frame with clockwise rotation, the deflection is to the left of the motion of the object; in one with anti-clockwise rotation, the deflection is to the right [5, 6].

Pressure sensors often rely on a sealed chamber and a deflecting diaphragm. Like other physical methods, it relies on either piezoresistive elements or a capacitive region to convert a pressure to an electrical signal. A difference in pressures on each side of a micromachined diaphragm will cause a deflection that can be directly related to the surrounding pressure [7-9].

As for the sensing of fluids, many types of mass flow sensing methods have been developed that integrate gas and fluid sensing to lab-on-a-chip systems [10]. Traditional methods of gas flow sensing at the microscale can be generally separated into two categories, thermal or mechanical, depending on the type of measurable response [11]. Thermal sensing methods can monitor flow conditions by either directly measuring the

temperature profile of a heated wire, or sampling the temperature of the medium around it. In the direct case, the element loses heat to the surrounding medium and its temperature is monitored as a response to flow [12]; faster flow corresponds to lower temperatures. This information is combined with known properties of the medium to find the flow speed [13]. In the indirect sensing case, the thermal profile of the flow is monitored near the heater and flow velocity is extracted [14]. The advantages of measuring the thermal behavior of the medium are that the heater and sensing element can be made in-plane, and the sensing technique is viable at the macroscale. However, a thermal gradient is required and the readings must be calibrated to the properties of a specific fluid.

Various mechanical flow sensing methods have been developed at the microscale using a wide range of mechanical [15], optical [16], and biologically [17] inspired techniques. Structures that show a measurable response based on mechanical interaction with the flow are most common. These mechanisms include cantilever deflection, differential pressure, resonating behavior, and deflection from lift force. Changes in resistance or capacitance correlate to properties of the flowing medium. Cantilever-based systems work by similar means to their macroscale counterparts. Deflection is caused by drag force on the structure and is correlated to flow speed [18, 19]. Direction can also be extracted with multiple sensing elements [20]. Differential pressure methods are based on pressure drop in a confined channel [21]. The difference in pressure across a channel can be examined by examining a pair of deflecting diaphragms at the ends of a known channel segment, a standard technique for pressure sensing. The pressure change can be correlated back to the fluid properties. Resonating structures also mechanically respond to the flow around them with a known response profile [22]. Lift force structures have also been

proven to react in a measurable way [23] and have been integrated with hot-wire techniques [24].

Disadvantages of mechanical sensors include sensitivity to particulate matter in the air, and unidirectionality with a single element. Air flow samples collected outside of the lab frequently contain particles upon collection. An exhaled sample from a living organism may contain liquid and solid components. Environmental samples contain pollen and airborne bacteria as well as silica and conductive particles. These contaminants can damage the sensing mechanism or cause false signals. The impact of particles can be lessened by minimizing the surface area normal to the flow direction, thereby reducing the cross-section for collision and deposition of particles. The use of lift force allows mechanical sensing with a small surface area normal to the flow. The suspended lift-force element is also separated from slow flow at the channel wall. Lift-based sensing structures have been developed in previous work, but retain the unidirectionality common to other mechanical flow sensing methods.

1.1.1 Microfluidic Sensing

While pressure driven flow is a mechanical phenomenon, systems that use a fluid medium at the microscale can be categorized as microfluidic-based. Many of these rely on a combination of electronic, optical, or chemical interactions to accomplish a task. A common example of an electronically monitored system would be a flow cytometer. While most technologies rely on electronics at some level, such as monitoring the resistance of a mechanically coupled element, cytometers have an electrical or optical signal that directly flows through the sample medium. Disturbances in the current can be related to event counts, such as the passage of individual cells or particles in a medium.

Blood tests are something that must be completed at high frequency in hospitals and doctor's offices around the world. These tests are carried out for a variety of reasons, from diagnostics to monitoring after surgery. One of the simplest and most commonly occurring tests is to determine the numbers of various cell types within a blood sample. A Coulter counter is the machine typically used in hospitals to perform this test. While the machine itself can run samples quite quickly, there are still many steps that must be taken to have the test completed. The test can be time consuming, and require large amounts of blood [25]. Due to the time constraints and blood sample sizes needed many groups are investigating MEMS devices for blood cell counting.

The two methods of counting particles and cells that are used most often are light scattering or aperture-impedance. A Coulter counter, most often used in hospitals, uses the aperture-impedance method. A typical Coulter counter can be used to count and determine the size of particles that are suspended in electrolytes. These devices contain microchannels between chambers filled with a blood sample, which can be considered a conductive

electrolyte solution populated with non-conductive particles because of the insulating cell membrane. As a blood cell flows through the microchannel, the electrical path is blocked, and the reduced current is detected. The amount of resistance change is an indication of the size of the particle [26, 27]. The devices are designed to use an AC signal that can sample to different depths within the cell membrane depending on frequency. Multi-frequency methods allows for both counting and classification of cells [28].

An example of an optical fluidic sensing technique can be seen with particle image velocimetry [29, 30] in MEMS channels. Particle Image Velocity (PIV) is an optical method of flow visualization that correlates a collection of images into associated velocity and fluid properties. Traditionally, particles monitored through PIV are seeded with tracer particles to enhance visibility and characterize fluid motion. Particle Image Velocity differs from other imaging techniques, as it can produce two dimensional and sometimes even three dimensional vector fields associated with particle movement, by comparing successive image sets. Particle concentrations within each image set makes it easier to identify individual particles, but cannot always be used to track particles between successive image sets, i.e. as seen in particle tracking velocimetry (PTV).

Chemical based techniques cover a broad range of sensing abilities that are often closely tied to biochemistry. This can include not only interactions with the medium, but chemically creating the microfluidic system itself with the use of chemically modified surfaces. One such example is in Surface Tensioned Confined Microfluidic (STCM) devices. The operation of STCM is primarily based on the interaction of fluids with hydrophobic and hydrophilic surfaces. With the proper preparation of a glass surface, a sharp wettability gradient can be designed to confine fluid flow. The sample moves along

by capillary action when the adhesive force of the liquid with the substrate is more than that with the edge [31]. Unlike some micro-scale projects, the working principles are not a small version of a macro-scale device. The containing pressure is small compared to many forces, and would not provide the same results at larger scales, but it has been shown that chemical reactions and mixing can take place in this setting [32, 33]. At the scale of the devices discussed in this thesis, surface tension plays a major role [34].

Many of the design principles that go towards a ‘dry’ MEMS system are also influential in the microfluidic realm. There are many examples where the fields of work overlap, such as in the fabrication techniques of Coulter counters [27, 35], or can merge to form a new methodology. For example, a material bilayers that are more traditionally used for thermal actuation [36, 37] have been appropriated as a structural material for a novel electroosmotic pumping system [38]. Aspects of microfluidics are influential within this thesis, and MEMS-fluid interaction is discussed further in Chapter 1.

1.2 Active Microfluidics and Actuators

Sensors are mostly composed of passive elements that react based on an input from the world. However, there are many instances where a user wants to incite the action on something at the microscale. For this task, MEMS actuators and active pumping techniques have been developed. There are a variety of microfluidic pumping techniques that are used to move a fluid medium through a channel or to a sensor. This technology has particular significance for biological samples that may require a medium to survive.

1.2.1 Microfluidic Pumping and Mixing

Methods of microfluidic pumping include electrokinetic and dielectrophoretic techniques, as well as pressure, ultrasonic, and thermally activated methods. Some fluids have useful electrical properties that allow them to be electrokinetically manipulated. In this case, these properties can be exploited to aid in mixing and movement. A periodic signal can be applied across a channel to alter the flow of the streams. If the two interfacing fluids have different electrical properties, the flow pattern can be varies from a laminar state some one that is more chaotic and conducive to diffusion in the case of mixing [39, 40].

Alternating flow patterns can be created using dielectrophoresis. Certain geometries will form flow vortices when their surfaces are electrically charged in an electric field. These patterns can change when the charge is reversed, allowing the streams to split and interact in a new way. This forced interaction and movement in different patterns will greatly increase mixing (as compared to diffusion) and can be used to create a net flow in a system [41]. Applications of dielectrophoresis have included the selective spatial manipulation and separation of bacteria, various cell types, and red and white blood cells.

The other aforementioned techniques are useful for speeding up mixing at the microscale. Pressure perturbation implies a state where streams being injected into a channel can have the pressure varied to change the interaction of the two fluids. At equal rates, side-by-side streams will form and have a single interface for diffusion down the center of the channel. If the pressure of one (and possibly both) is pulsed or changed in a periodic fashion, the area of the interface between the two streams can be greatly increased. This allows more surface for diffusion to occur [42, 43].

Ultrasonic and thermal methods can be used to enhance mixing by affecting an air bubble. Changes in temperature or applied pressures can cause pulsing to pump or mix a medium. In each case, this changing condition will lead to increased energy and mixing in the microfluidic device [44-46].

1.2.2 Microactuators

There are a multitude of actuating schemes that have been developed to manipulate objects at the microscale. Types of actuators can be grouped into three categories (high, medium, and low), by the level of pressure that they can generate. The highest pressure potential lies with stacked piezoelectric actuators. This type relies on materials that have a high Young's modulus and expand and contract based on the type and magnitude of voltage applied across the bulk. These are most suitable for applications that require large forces [47, 48].

The medium pressure range includes techniques such as pneumatic [49-51], thermopneumatic [52], and shape-memory alloy [53, 54]. Pneumatic actuation involves using a pressurized air flow to deflect a diaphragm or fill a chamber, thereby causing net movement in the system. In the case of thermopneumatic actuators, this air pressure is

brought on by the expansion during the state change from liquid to gas in a reservoir. The evaporation is caused by heating, hence ‘thermo.’

Shape memory alloy (SMA) actuators undergo phase transformations from a ‘soft’ martensitic state at low temperatures to a ‘hard’ austenitic state at higher temperatures. Applications of this property are based on its ability to return to the original state with a temperature change. Thermomechanical actuation also falls in this category, is discussed in detail in the following section, and is a critical aspect of the work in this dissertation.

Low-pressure actuating types include electrostatic [55-57] and electromagnetic [58, 59] actuators. The more common of these is the electrostatic method based on attraction between two oppositely-charged plates. Their operation is based on Coulomb’s Law; it defines the force between charged particles. This principle is most simply applied in a parallel plate capacitor, and is expanded as the MEMS comb-drive actuator, a more complex geometry that arises from the need for motion in the plane of the wafer, and from the limitations of planar microfabrication fabrication techniques.

A commonality with many of the many actuation techniques is that they require a physical wired connection to feed an electrical signal into the system. For some devices this direct connection is unavoidable, but for those that are thermally based, there are other options to provide heating by other methods than Joule heating with applied current. For example, the surrounding environment can be heated, or a targeted light source can be used to add thermal energy. Stimulating devices with laser light offers a versatile wireless medium for powering such devices.

1.3 Light-Driven Thermal Actuators

Light-induced actuation based on plasmonic heating is similar to existing thermally driven types of actuators such as thermopneumatic, solid-expansion, and bimetallic. The basis for these devices is the thermal expansion of a material; some type of heating is applied to exploit the material properties of the actuating medium with known response to temperature change. In general, optically-actuated MEMS structures respond proportionally to their absorption of the incoming light energy. Under continued exposure, a photothermal device will heat up to reach equilibrium with the surrounding environment. The extent of actuation is based on the physical properties of the heated material, such as its thermal expansion coefficient and modulus of elasticity.

Geometry can be designed to exploit thermal expansion in devices that demonstrate large displacement and moderate force compared to other MEMS techniques. There are advantages and disadvantages to integrating a light-driven functionality with these mechanisms; this topic will be discussed further in the next section.

Solid expansion offers high force compared to other micro-scale actuation techniques [60]. Often the displacement of this type of actuator is low, but such devices can act as a lever to overcome this limitation. Absorption-based actuation is a sufficient option for this method. Generally a single absorbent material is doing the actuation so the heating would be direct, as opposed to a resistive electrical trace that might act on another material with a large expansion coefficient. The added bulk required for more complicated expansion-based structures is detrimental to the heating of the system, and the response time suffers from the thermal capacitance. A larger thermal mass requires more time to heat and cool, which directly translates to the response time of the system.

Bilayer systems offer large out-of-plane displacement with a thin-film based structure [37]. They can even be designed to push on other elements to create a nearly horizontal architecture [61]. This out-of-plane fabrication style is more appropriate than thin planar films for light-based actuation, because thin suspended structures exhibit a faster response to temperature than a bulkier planar solution. Phase change can also be used to generate rapid transitions [62]. These systems have a near-instantaneous response to joule heating, which cannot be physically matched by optical heating which is restricted by the surface absorbance. However, the potential for large displacement is restricted by the need to make electrical contact for that method, and the selection of materials is limited to those with a rapid phase change. Optical energy transfer removes this restriction at the cost of response time.

In the realm of other technologies, thermal actuators are not the most efficient available. A comparison of many actuator types was gathered and can be used for comparison [63]. The data suggests that electrostatic and piezoelectric actuators are far more efficient than thermally driven systems. This high efficiency is due to these methods using other physical phenomena that do not rely on temperature conduction for their operation; energy lost to thermal dissipation cannot be recovered, but energy stored in a capacitor or elastic structure can be recovered. However, because optically-driven thermal actuators apply to a wide range of material and fabrication systems, they offer many practical advantages. This work looks to improve their performance and include their functionality in microelectromechanical systems.

1.4 Bistable Geometry

Devices with bistable geometry offer the advantage of requiring power only when changing mechanical configuration. This behavior is critical for applications that require mechanical actuation in power-limited situations. The function of a bistable structure is to have two discrete stable states that can be selected by application of an external stimulus, such as heat, vibration, electrostatic fields, magnetic fields, or pressure. The devices maintain their new state without a continuous power input which leads to a substantially lower time-averaged energy consumption than active devices. Bistable MEMS have been used for a variety of applications such as electrostatic and optical switches [64, 65], magnetic actuators [66], micro-valves [67], pressure-actuated switches [68], multiplexing switches [69], and cross-bar latches [70]. Bistable thermal actuators have been shown to perform well with optical systems for they have a relatively large deflection and use MEMS bulk micromachining techniques, enabling low cost fabrication with a high percentage yield [71].

1.5.1 Buckled Beam Theory

A simple system can first be examined for further insight into bistable behavior. Buckled beams are a well-researched and useful structure in MEMS. Most simply, a beam is compressed between two anchors, and a switching behavior is created because of the strain in the structure. If the beam was a perfect cylinder the deflection direction could not be predicted. However the planar nature of microfabrication leads to rectangular beams with non-uniform width and height parameters. In-plane motion is achieved by having beams with greater thickness than width, so bending occurs on the axis with less resistance to deflection. Several groups have made use of this phenomenon to design sensors and

actuators. For example, Qiu et al. [72] used a similar technique with coupled parallel beams to make a bistable switch. This beam displayed a similar behavior experimentally to the theoretical switching behavior explained in this report. Charlot et al. [73] demonstrated the scalability of this technique and ability to sense the state of the beam in their work for memory applications. A deflected nano-beam acts as a memory bit, and the state is read by electrode capacitance located near the beam deflection extents.

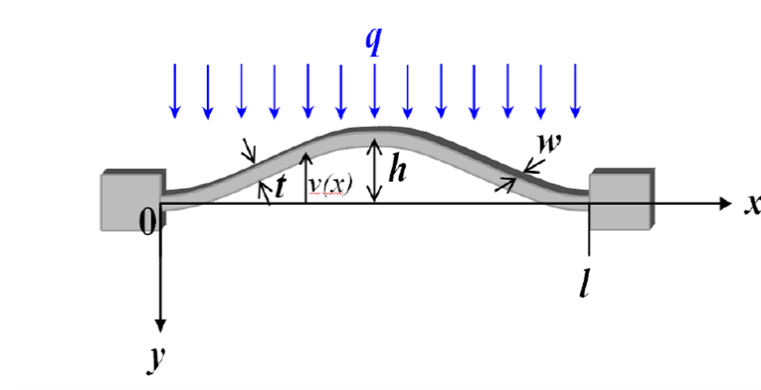


Figure 1- A typical compressed beam structure. The beam is suspended between two anchors [74].

The theoretical modeling of this system has been well-documented. One of the more common citations for this behavior is the model for MEMS application presented by Vangbo [75]. In-depth development of the theory has also been shown by Park [74]. The relation that governs the suspended beam is shown in Equation 1:

$$EI \frac{d^4 v}{dx^4} + P \frac{d^2 v}{dx^2} = 0 \text{ Equation 1}$$

In this case, v is the y -displacement of a point on the beam x , more accurately shown as $v(x)$, and P is the total applied load. This equation can be solved to provide a non-trivial sinusoidal solution. The mathematical details of this displacement solution and the bending moment M are contained in the work by Park cited above. In general terms, the load is

considered to be perpendicular to the beam and suppresses higher order components of the displacement, leaving the main amplitude term a_1 . The potential energy U stored in the beam can be calculated by integration over the beam with known force, strain, and bending moment parameters. The resulting equation for energy U stored in the beam is:

$$U = \frac{3EA\pi^4(a_1^4 - 4ha_1^3 + 4h^2a_1^2)}{64l^3} + \frac{\pi^4 a_1^2 EI}{l^3} - q \frac{a_1 l}{2} \quad \text{Equation 2}$$

This can be solved by assuming that the center amplitude a_1 should minimize the strain energy U under applied force q . In other words, solving $dU/da_1=0$ results in the following relation between the applied load and beam amplitude. This relation is shown in Figure 1.

$$q = \frac{3EA\pi^4(a_1^3 - 3ha_1^2 + 2h^2a_1)}{8l^2} + \frac{4\pi^4 a_1 EI}{l^4} \quad \text{Equation 3}$$

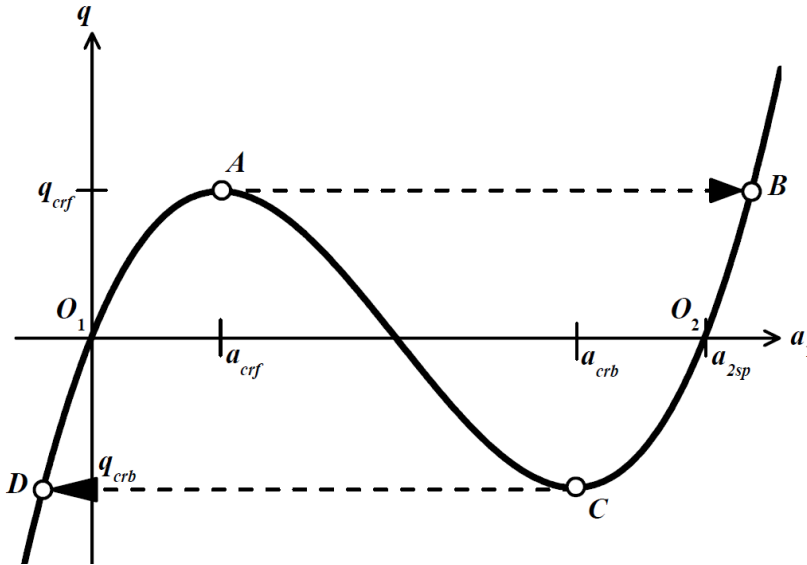


Figure 2 - Characteristic S-Curve associated with bistable compressed beams [74]

The diagram in Figure 2 shows the relative force-vs-displacement curve associated with a bistable compressed beam. The points along the horizontal axis O_1 and O_2 represent the configurations with local minimum strain in the beam. Multiple displacement

possibilities with the same force range indicate that the structure is bistable. It is seen that within a certain force (q) range, the beam deflection is proportional to the applied load. On the plot, this is the arc between D-A and C-B. The beam will revert to the nearest minimum strain state (O) if the load is removed. In this way, the compressed beam is bistable, and able to stay in one of two states without external input.

The transition region between A and C is not physically realizable as shown in the graph. When the beam is at stable state 1 (O_1), an applied critical forward load (q_{crf}) will rapidly transition the system from point A to B. Likewise, when the critical backward load (q_{crb}) is applied to a beam in state two it will rapidly deform to the amplitude at point D. The critical amplitudes at the brink of a state change are labeled above as a_{crf} and a_{crb} for forward and backward amplitude, respectively. The extension to the left of D and right of B represent further stretching of the beam eventually leading to critical deformation and fracture.

1.5.2 Bistable Out-of-Plane Structures

This theory can be extended to more complex geometry. “Pop-up” architecture has been used to make bistable devices such as a bistable windowpane structure. The shape presents with two stable configurations as seen in Figure 3. The device will randomly conform to one of two symmetric shapes upon release from the substrate during fabrication.

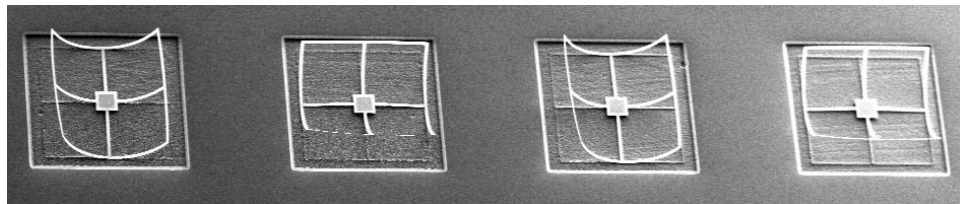


Figure 3 - SEM view of the bistable windowpane structures, released to one of two states.

The bistable nature of the sensing device is clearly expressed in the row of devices above. The stable states are seen to alternate in Figure 3. The shape will conform to one of two shapes upon release from the substrate during fabrication. The three dimensional geometry used in this is created from a bilayer of silicon dioxide and platinum. The material strain responsible for the shape is created during fabrication and is heavily temperature dependent.

6 A MEMS – Gold Nanoparticle Hybrid

Structures such as the one in Figure 3 require a more complex control scheme than bulk heating to change them into a controlled state. However, the three-dimensional nature makes Joule heating difficult because of the requirement of physical wiring. Light-based heating is ideal for this situation, as it requires no physical connection. However, without a mechanism to confine the light-based heating to certain areas, the light will not provide a controlled switching behavior; it only allows random chance to act in the same way a state is selected at fabrication. To add controlled-switching functionality, it is proposed in this work to selectively pattern the device surface with gold nanoparticles to produce thermal gradients in the regions that are intended to induce specific switching.

Chapter 2 details mechanical interactions of bilayer pop-up structures with different types of forces. Biological integration of this light-actuated technique will require a structure that can successfully apply forces and be subjected to a fluid flow without damage to the device. The first sections describe using the bilayer for containment and controlled interaction with a microbubble. Results provide insight into the elastocapillary length and flexibility of the MEMS component in a fluid medium. The second half of chapter two examines the reaction of a structure in a moving fluid. This combination of experiments details the aspects of the project that are critical to interaction with biological components such as cells and nerve endings, as well as the survivability in flowing mediums such as in vessels and lungs.

Chapter 3 investigates the feasibility of adding gold nanoparticles to increase the efficiency of a surface's nIR absorption. In this work, it quantifies the impact of these particles on a platinum surface, and documents a technique for deposition onto a solid

substrate. These two components are critical for meeting the end goals of this project. An efficiency increase must be established to make the technique useful, and the method must be compatible with standard cleanroom processing techniques so it can be applied to a complex range of MEMS sensor and actuator technologies.

Chapter 4 expands the scope of a patterning a surface by comparing the performance of particles that are tuned to different wavelengths. This theory is paramount for establishing more sophisticated control over photothermal actuation than simply increasing laser power or duration. Wavelength-specific patterning will allow for controlled thermal gradients to be created, opening the possibility of new switching, pumping, and asymmetric actuation techniques in a thermally driven system.

Chapter 5 details the convergence of the previously described work. An out of plane thermal actuator is coated with particles and the mechanical actuation is stimulated by a nIR laser. The response is monitored and deflection is estimated from captured images of the movement. Experimental evidence is provided to support a laser actuated structure with enhanced absorption caused by gold nanoparticles.

Finally, Chapter 6 provides a summary and concluding remarks on the overall project. Future directions and improvements are proposed to expand on this body of work.

CHAPTER II

MECHANICAL CHARACTERIZATION OF BILAYER STRUCTURES

The structure for the light-driven microactuators is a material bilayer. The composition, fabrication, and structural analysis of this architecture are important for the design of thermally actuated MEMS devices based on this technique. Interaction between fluids and these structures has been examined to experimentally characterize the bilayer component of this project. Two application platforms were examined. In the first, submerged bilayer structures were used to contain microbubbles and analysis gave insight into their elastocapillary length. That is the radius of curvature that produces equilibrium between interfacial energy and strain energy in a filament that contacts an interface. Second, bistable pop-up structures were exposed to flowing gas. There was a mechanical response because of lift and drag forces that can be related to the spring constant and strength of these devices. The following sections detail these laboratory examinations of bilayer interactions.

2.1 Bilayer Interaction with Microbubbles

The first investigation outlines work towards generating and controlling microbubbles as protective “lids” for samples collected from the environment. The fabrication method uses “strain architecture” to construct three-dimensional cages with high surface area. These structures confine the bubbles and perform as electrodes for electrochemical sample collection and electrolysis-based gas bubble generation. The focus of this section is on the interaction between the microcages and generated bubbles, including the bubble generation mechanism, bubble growth rate, response to hydrostatic pressure, effect of interfacial-tension modifying coatings, and long-term stability.

2.1.1 Motivation for a Bubble Shield

Gas-trapping microstructures have evolved on plants that develop superhydrophobic surfaces [76] to create a controlled air-water interface. Such structures use geometry at multiple scales to make a tent-like bubble layer as on the fern *Salvinia* [77]. In microfluidics, bubbles have been used for numerous applications such as particle sorting [78], inkjet printing [79], and implementation of Boolean logic [80]. Bubbles can also be detrimental, blocking flow in microchannels [81] and interfering with electrophoretic applications by blocking signals and altering fluid flows [82]. They are an unwanted byproduct of electroplating. In all these situations, methods to control and trap microbubbles are of interest.

The devices referenced in this section of the thesis consist of a metal electrode that is energized to plate out trace metals from natural water sources. The collected sample is returned to the lab for analysis. If left in the field unprotected, a biofilm will form on any electrode surfaces exposed to the water [83]. This film will block reactions between the

surface and surrounding solution. A gas bubble could protect the metal surface from water until testing, and then preserve a collected sample from contamination. Such an array of bubble-lidded microcontainers is illustrated in Figure 4, where a series of metal-lined cages is sequentially exposed to the environment. After releasing a trapped bubble and collecting a sample on the cage walls by electroplating from solution, the bubble is regenerated. The result is a time-stamped archive of the chemical environment.

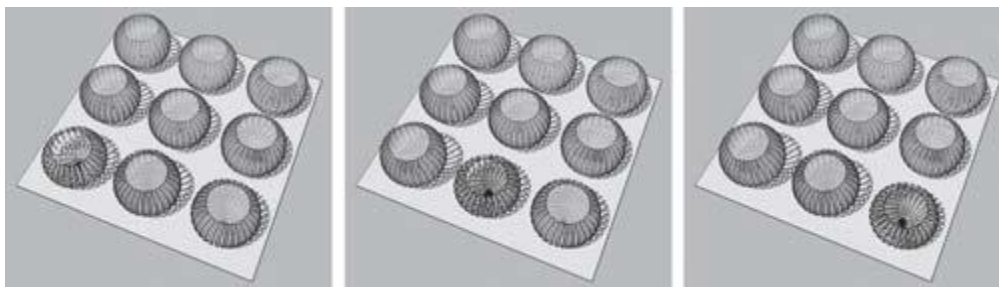


Figure 4 - Array of 300 micron diameter bubble traps undergoing an electroplating sample collection sequence across the front row.

2.1.2 Microbubble and Trap Theory

Stress-mismatched metal-oxide bilayers form three dimensional (3D) microcages that serve as plating electrodes in the system. Their interaction with bubbles can be modified by changing the surface wettability and cage geometry. The devices are fabricated with a two mask metal and oxide process that has been documented by Moiseeva et al [37].

Figure 5 shows a two-dimensional (a) microcage layout, (b) optical, and (c) electron micrographs of released cages, and arrayed cages within (d) sample wells allowing access to contact pads. The transition from planar to a 3D structure only at the last step means that bubble-generating electrodes can be integrated at the base of the cages in one step (Figs. 2(a) and 2(b)). This geometry is more difficult to achieve by bulk micromachining, in

which features are etched in thick layers of silicon. The result is that bubbles can be electrolytically “inflated” from points inside the cage.

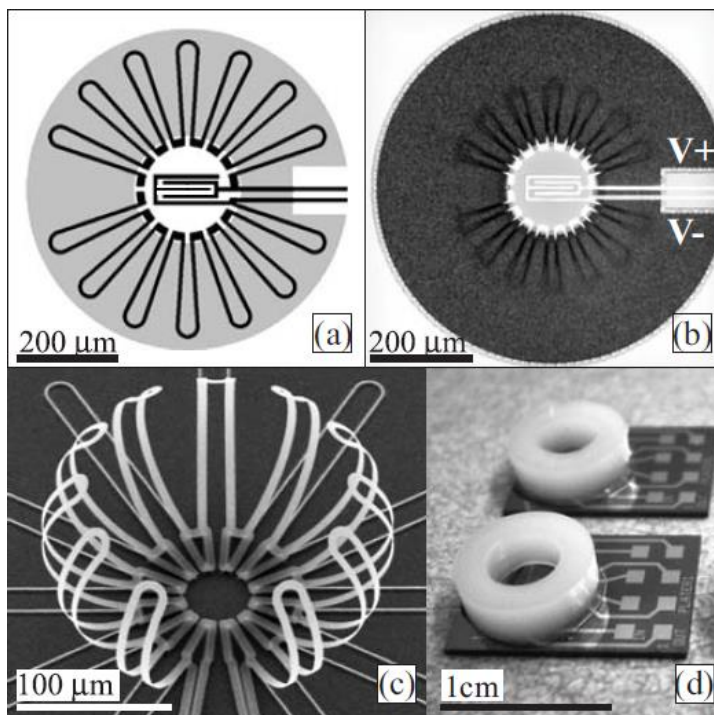


Figure 5 - Released cage devices used for bubble generation and trapping.

Electrolysis of water occurs at voltages above 1.21 Volts, which is within the operating range used for electroplating with these devices. However, it is not energetically favorable to form oxygen at until 1.8-2.55V on metal electrodes [84]. This threshold is an advantage in applying the cages to electrolytic sample collection of trace metals, because it reduces bubble formation during routine electroplating.

Heavy metal analysis is commonly performed at low (.1 to 1) voltages [85]. These potentials can be applied as long as needed to get a sufficient film on the electrodes. The film growth rate is dependent factors such as the surrounding metal concentration and the deposition time. The electroplating routine may range from five minutes [86] to the order

of an hour [87] depending on the application. These low potentials across electrodes are insufficient to create bubbles capable of shielding the surface. This allows for independent bubble growth and electroplating stages of the device operation.

Maximum gas volume (hydrogen plus oxygen) vs. time is described in Equation 4 for 100% efficient electrolysis:

$$V_{gas} = V_{H_2} + V_{O_2} = (3RTIt)/(4FP) \quad \text{Equation 4}$$

where T is temperature, R is the universal gas constant, I is current, t is time, F is the Faraday constant ($F = 96485 \text{ C/mol}$), and P is absolute pressure. However, actual efficiency is reduced by dissolution of oxygen and hydrogen back into solution instead of into the bubble, as well as electrode configuration [88] and ohmic loss in the aqueous solution [89]. In the bubble trap structure, the efficiency is much below the theoretical maximum.

2.1.3 Experimental Methods

Experiments were conducted at voltages ranging from 2.5 to 3 V. The electrodes were set at a constant voltage for 20 minute intervals, and the applied current and bubble growth were recorded through LabVIEW software and time-lapse photography at 6 frames per minute. The images were analyzed for bubble diameter, which was converted to gas volume. By comparing the experimental results with the ideal gas volume equation, the efficiency of the water electrolysis can be determined. Figure 6 compares Equation 4 with the experimental results and shows images of bubble evolution at different stages during growth; a fit to the results gives .8% efficiency for electrolysis-based gas generation.

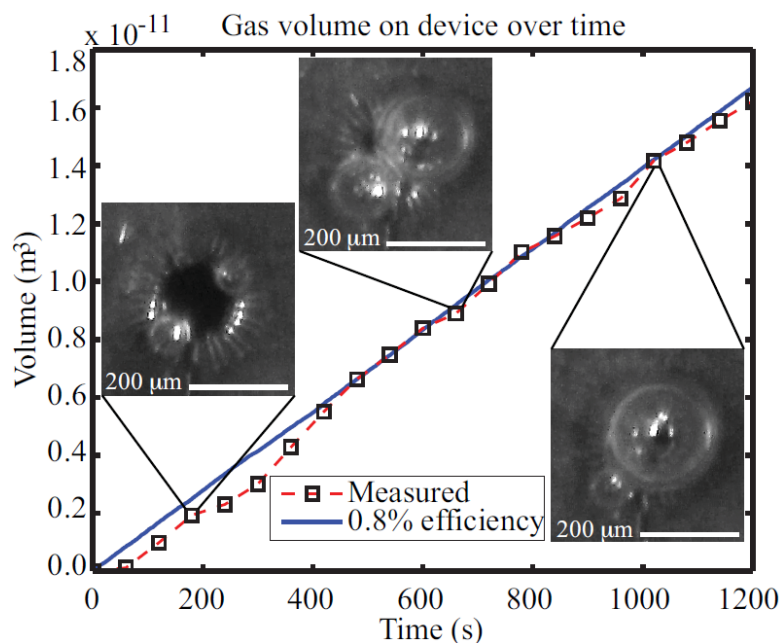


Figure 6 - Measured bubble volume present over 20 minutes plotted beside the ideal gas law predicted generation at 0.8%.

2.1.4 Analysis of Bilayer-Bubble Interaction

Bubble volumetric growth is linear with time, and the power input is in the tens of nanowatts. With currents in the 10-20 nA range, and voltages below 3V, the electrical requirements are well within the resources of a battery-powered autonomous sensor array. At 2.7 V it takes approximately four minutes to fill the microcage. Bubbles nucleate at random points within the cages, which have a metalized inner surface and a hydrophilic oxide outer surface. As they grow, the hydrogen and oxygen bubbles merge and move to the center of the cage. Growth self-terminates if the bubble completely covers the metal and prevents it from further reacting with the water. Octadecanethiol (ODT) was applied to the device surface in some cases. This self-assembled monolayer rendered the metal

hydrophobic and bubbles adhered to the surface longer than on a non-coated device, in agreement with previous work [90].

Figure 7 is a time series of a bubble confined to a cage as the hydrostatic pressure is increased. Pressure was varied by sealing the sample well, then connecting the chamber through tubing to a regulated nitrogen tank. As the pressure is increased, the filaments conform to the shrinking bubble surface until the force needed to bend them can no longer be supplied by the interfacial tension of the bubble.

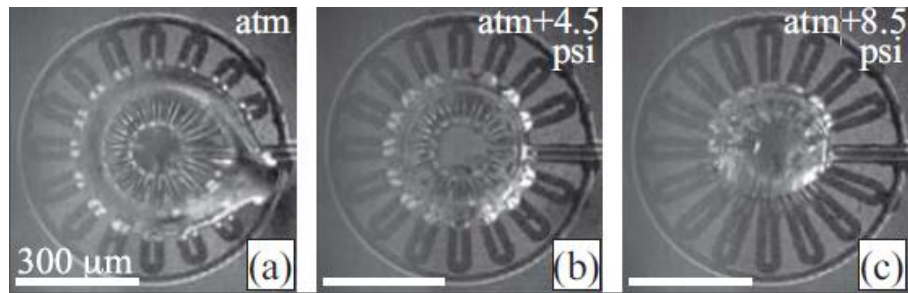


Figure 7 - An air bubble trapped in a microcage in water. The filaments conform to the surface of the bubble over a range of bubble diameters. The outline of the original etch pattern remains on the plane of the substrate, while filaments fold around the bubble.

2.1.5 Insight into Elastocapillary Length

The elastocapillary length $L_{EC} = (B/\gamma)^{1/2}$ is the radius of curvature that produces equilibrium between interfacial energy and strain energy in a filament that contacts an interface[91]. Here B is the bending rigidity $Eh^3/12(1-\nu^2)$, γ is the interfacial tension, E is Young's modulus, h is the filament thickness, and ν is Poisson's ratio for the filament material.

In the structures of Figure 7, the elastocapillary length of ~ 120 microns is in the same range as the 150 micron cage radius and the overall filament length. Thus the filaments are

short enough that they are not immediately destroyed by surface tension, yet are compliant enough to be strongly deflected by the bubble.

The cages have been observed to retain bubbles for a week, in contrast to bare gas bubbles in equilibrium with a solution. Bare bubbles not in contact with a surface are known to have a typical lifetime measured in minutes, with bubbles larger than a critical radius accumulating gas and floating to the surface, and bubbles below the critical radius diffusing gas into solution and dissolving completely. For oxygen in water near saturation, the critical radius is in the range of 100 microns [92]. The cages here (100 to 300 micron radius) exceed the critical radius and are in the growth regime.

Trapped bubbles must be released to expose fresh plating surfaces. Overinflated bubbles were observed to escape cages with triangular cross-sections by opening the filaments. These interdigitated structures could serve as release valves on the side of a spherical cage.

Microcages with electrodes can stabilize a bubble against both growth and shrinkage, refilling a shrinking bubble by electrolytic gas generation. They can slow the growth of a bubble by forcing a high local curvature (high surface energy) between the filaments where the growing bubble makes contact with the surrounding water. By stabilizing a gas pocket over a surface, these microcages could be useful in underwater chemical sensors that require diffusional contact with dissolved gases. Such structures are also able to re-inject gas by electrolysis if the water level rises and increases the hydrostatic pressure, shown in Figure 7.

These advances will improve aquatic sampling platforms in which bubbles are generated through existing electroplating contacts at a higher potential, without additional structures or mechanical parts. Once created, the bubbles are stable at a size large enough to

protect a majority of the plating surface—providing surface-passivation options for low-power autonomous sample collection and archiving.

2.2 Bistable Bilayers Subjected to Lift and Drag Forces

The second experiment uses a bistable 3D MEMS structure for application as a bidirectional gas flow sensing. This switching mechanism is fast, repeatable, and requires no additional input power. This sensor is suitable to energy-starved applications such as wireless sensor nodes where low energy consumption is critical. An array of such sensors could provide a no-power passive memory bank for no-power storage of threshold flow levels for an indefinite amount of time before the device is retrieved. This sensor adds new low power functionality to the methods available for air flow detection in aeronautical, environmental, and medical systems, including lab-on-chip systems that monitor gas flows in anesthesia and respiration.

For this exploration, a lift-force based mechanical sensor for recording flow speed and direction from a single structure has been envisioned. Minimal surface area is presented to the oncoming flow before flipping from one stable state to the other, drastically reducing the impact area for particulates and reducing the need for additional on-chip components to filter the air flow. This novel structure also incorporates a directional element within a single device to further reduce the system footprint compared to systems that need multiple sensor elements to determine flow direction, and it interacts with the flow a distance above the surface to avoid the no-slip wall condition. The sensing range can be modified by altering the device parameters that dictate the lift coefficient of the geometry. Unlike previous mechanical devices that operate in a continuous bending mode, the structure has two mechanically stable states which serve to archive a sensed flow velocity indefinitely without power consumption.

A schematic of the sensing principle is shown in Figure 8. The device at rest will deflect with an air flow in any direction, but only shows a state transition when applied parallel to the curved plane. The device orientation is mechanically switched if the energy threshold between stable states is overcome by the lift force acting on the device. This flow speed threshold is recorded by mechanical change of the structure. A perpendicular flow does not cause the state to reset, and the event is recorded until the device is reset with a flow of the same magnitude but with a 90 degree rotated flow direction, as demonstrated in Figure 8. The device threshold can be adjusted by changing the surface area impacting the lift force or by modifying the device dimensions to change the bilayer stiffness.

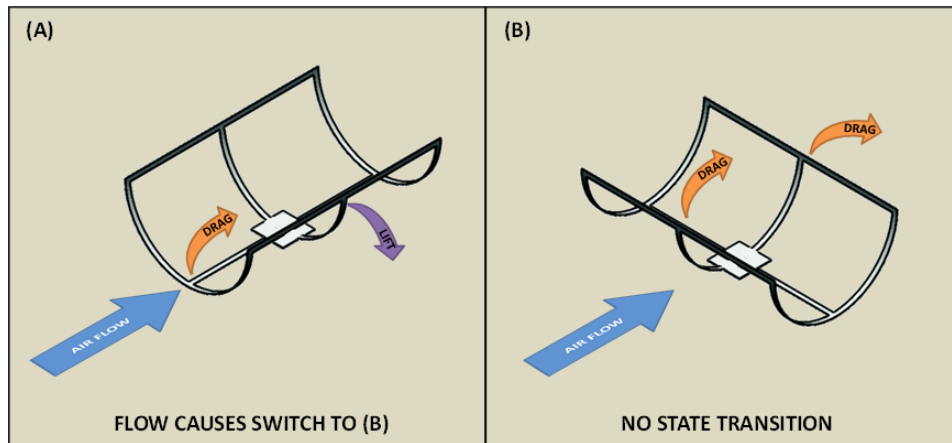


Figure 8 - Schematic view of the bistable windowpane device used in this work. Air flow along the down axis will cause a deflection to the other stable state. The transition is only reversible if the air flow direction is rotated 90 degrees.

2.2.1 Windowpane Theory of Bistability

The three dimensional geometry used in this device is created from a bilayer of silicon dioxide and platinum. A stress mismatch between the two materials causes the structure to deform out of the plane with a well-defined radius of curvature [36]. The

material strain is created during fabrication and is heavily temperature dependent because it is based primarily on the difference between the thermal expansion coefficients of the bilayer. As discussed previously, these bilayer structures have been used to interact with fluid and gas at the microscale [93].

The windowpane shape used for this investigation presents with two stable configurations [20]. The device will randomly conform to one of two symmetric shapes upon release from the substrate during fabrication. These two stable orientations are shown as they correspond to the net energy stored in the structure in Figure 9.

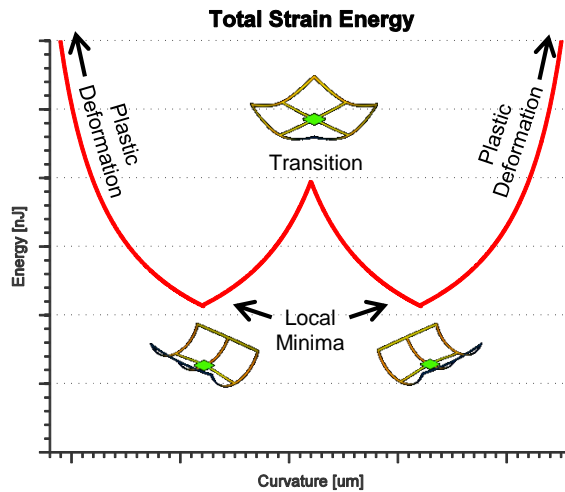


Figure 9 - Potential energy estimation in the bistable windowpane. Switching occurs at the central peak and stable states are at the two local minima.

The bistable nature of the sensing device is illustrated in the energy diagram. The stable states are seen as the minima in the graph. These points correspond to the windowpane structure curved parallel to either the horizontal or vertical in-plane axis. The shape will fall to rest at the nearest local minimum if no additional energy is applied.

Structures with a square side length of 550 μm to 700 μm at 25 μm intervals were fabricated to characterize the effect of surface area on the lift force, and therefore flow speed. The lift force is:

$$F_L = (1/2) \rho v^2 c_L A \quad \text{Equation 5}$$

The lift force (F_L) is proportional to the density of the medium (ρ), the flow velocity squared (v^2), the lift coefficient (c_L), and the surface area (A). The force enacted by a flow was changed by modifying the side length parameter, which is a component of the surface area.

2.2.2 Suspended Bilayer Fabrication

The devices for this project are fabricated with a two mask cleanroom process.

Figure 10 is a fabrication diagram for the complete cleanroom process.

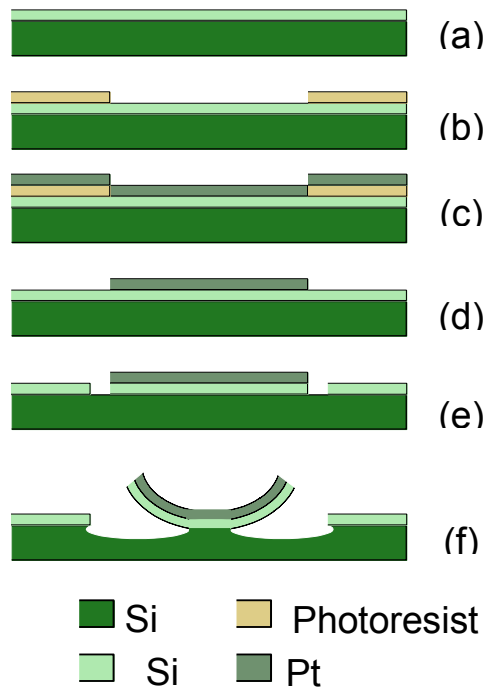


Figure 10 - Fabrication diagram for the cleanroom process used to fabricate the wind sensing devices.

A standard 4 inch silicon wafer acts as the substrate for material deposition. The bilayer required for creating the pop-up geometry is created by first thermally growing a 500nm SiO₂ layer on the substrate (a). Photoresist is then deposited and patterned to mask the surface for the metal deposition (b). Next, a 10nm/90 nm titanium/platinum (Ti/Pt) layer is deposited by sputtering (c). The features are defined by lift-off of the previous patterned photoresist (d).

A second photomask is used to define where the SiO₂ will be etched to make windows to the silicon. The exposed photoresist and patterned metal act to mask areas of the SiO₂ while the wafer is exposed to a reactive ion etch to create open windows to the substrate (e). Finally, the openings allow an isotropic XeF₂ etch of the silicon that releases the strained bilayer from the surface (f). The final resulting structure curls to one of two states as pictured in Figure 11.

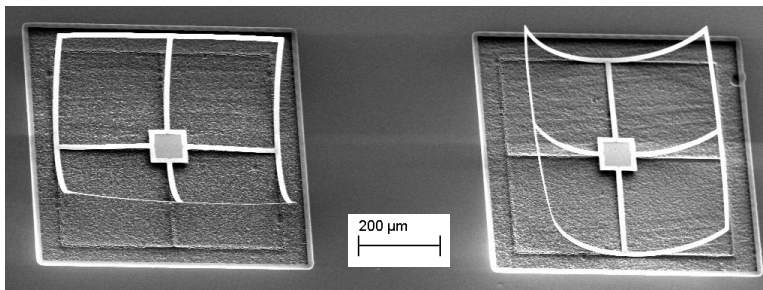


Figure 11- Schematic view of the bistable windowpane device used in this work. Air flow along the down axis will cause a deflection to the other stable state. This is only reversible if the air flow direction is rotated 90 degrees.

2.2.3 Method of Applying Flow to a Pop-up Element

A micro wind channel was created for testing these devices. Figure 12 shows the micro wind tunnel opened for exchanging the device die. Pressurized N₂ was used for the

flow medium. The gas was applied to a single channel with a centrally situated device. The fabricated wind channels are at 90 degree intervals to allow testing of the full switching range. The devices were optically monitored via an Olympus BX-71 microscope for a change in state with a 1 second air burst at a known velocity. The device will reliably switch in both directions at or above a flow speed threshold depending on the geometry.

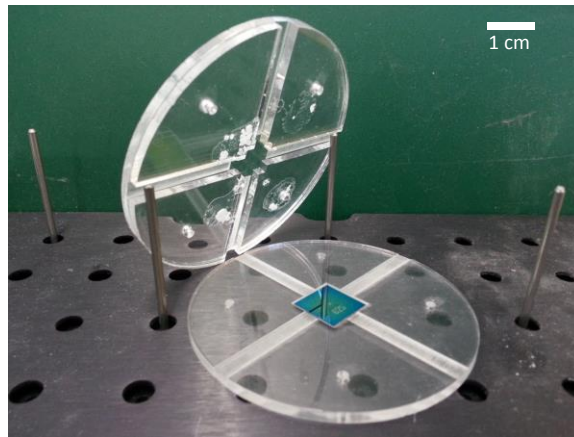


Figure 12 - Picture of the wind tunnel used for experiments with the wind sensor. The top can be removed to allow the test chip to be changed.

The wind tunnel is laser cut out of three layers of 1/8th inch (3.175mm) acrylic. Straight cut and raster modes are used to create the air channels and seating area for the device. The inlet and outlet channels are 5mm wide with an approximate height of 3.2mm including the raster etch. Plastic tubing is installed in these channels for air flow into and out of the system. The center device chamber is a 1cm square with a height of 3.175mm from substrate surface to the chamber ceiling. A 500 μ m raster etch of the center base was included so the substrate surface was even with the chamber bottom. The air flow in the

center device area is calculated to be laminar. The flow speeds with air used in this experiment, 5 to 10 LPM, suggest a Reynolds number range from 800 to 1600.

2.2.4 Discussion of the Force Interaction

The data shows that the air flow required to cause a state change is reduced as the surface area of the device increases. There are multiple explanations for this behavior. First, elongating the side length increases the surface area of the structure. Lift force is proportional to this area for a constant air speed (A in Equation 5), so larger devices experience more lift. Second, the stiffness (k) or spring constant of the beams is inversely proportional to the square side length which results in more deflection with an identical force as length increases.

These two conditions indicate that the flow speed required to induce a state change will decrease with increasing side length. A longer side length will produce more lift and be less stiff, therefore requiring a lower flow speed to meet the energy threshold in bistable operation. The inverse also holds true, a smaller device will require a larger magnitude flow to cause a state change in the system. In all cases, the device will deform under a flow but will return to the initial orientation once removed if the energy threshold is not met. The experimental correlation between side length and critical flow speed is displayed in Figure 13.

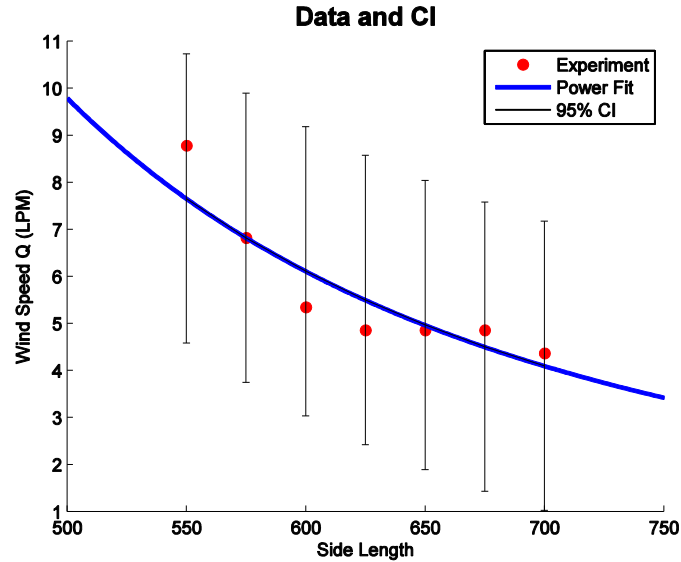


Figure 13 - Data relating the side length of the folded windowpane with the air flow speed required to cause a state change.

The measured results verify the expected trend of the data. The data shows that the threshold can be adjusted by changing physical parameters of the device. This is important for the tunability of the system. An array of these structures could be used to monitor and store an even event occurrence at various levels. Currently the detection of a state change is not automated, but the metal-oxide structure of the device may allow for capacitive measurement between the structure and surface [94]. The large deformation seen in this device also lends itself well to simple image processing for automated reading of an array of elements.

2.2.5 Applying This Device to Air Flow Sensing

Numerous air flow sensing techniques have been developed at the microscale, and often the appropriate sensing method is the one that most facilitates the particular sensing as needed per application. The preceding discussion has outlined a lift-based bistable MEMS structure for recording and archiving flow speed and direction. An advantage

over current technologies is that the device has minimal surface area facing the oncoming flow so particulate build-up is highly minimized. This three-dimensional structure responds to the flow at a distance above the surface and also records direction information. This work has shown that the flow speed threshold can be tuned by modifying the device parameters that impact the device stiffness and lift force generated. This technology may allow for new air flow sensing techniques on a miniature scale that are more resistant to contamination and require less power than current methods.

2.3 Monitoring a Suspended Element

There must be a way to interface with a MEMS sensor for it to be useful. Electronic methods have been traditionally used to monitor mechanical changes in a structure. This includes measuring the capacitance of a gap or resistance of a physically or thermally strained element [94]. Optical methods of data collection have become more viable in the last decade. Imaging at a sub-micron level has become a feasible route because of increased pixel density in CCD arrays. The following discussion investigates the feasibility of each method for the windowpane structure.

2.3.1 Electronic Sensing

Monitoring the system electrically is possible in theory but would rely on the ability to measure capacitance in the pico or femto range. However, it would require nanometer precision to on the release of the devices to create the gaps required. Figure 14 shows the potential circuit to be created:

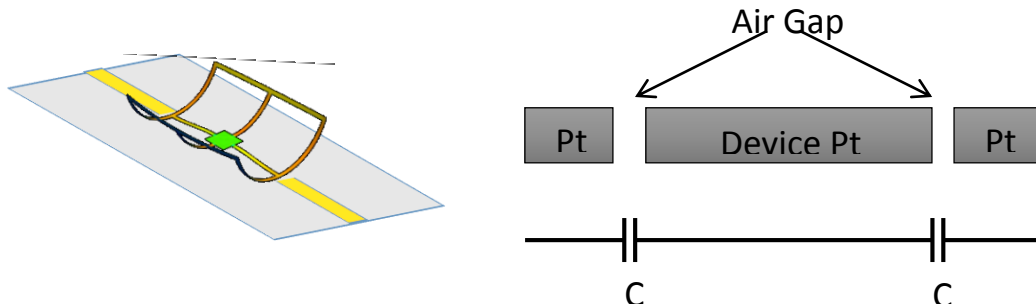


Figure 14 - Physical layout and circuit diagram for capacitance measuring across a released device

These difficulties are present because of the platinum trace dimensions. In this case the electrode area for calculating capacitance is 200nm x 20 μ m. The gap between the surface

circuit and released device would have to be sub-nanometer to achieve a measurable capacitance. Electrically monitoring the status of these devices is not ideal for this reason.

2.3.2 Optical Detection

Optical detection would be more suitable for reading an array of these devices, and has been used in other work with similar actuating structures [95], switches [96], and sensors [97]. There are two methods that could be utilized to read the state of these sensors. The first method would be to have a single line of devices and shine a laser parallel to the surface. The device has two definite states that are 90 degrees shifted. This means that one orientation will block light, and another will allow it to pass. Figure 15 demonstrates this concept with a single device. To use this setup with multiple devices, there could only be one row of structures that would be perpendicular to the laser direction. This limits the amount of data that can be collected per area.

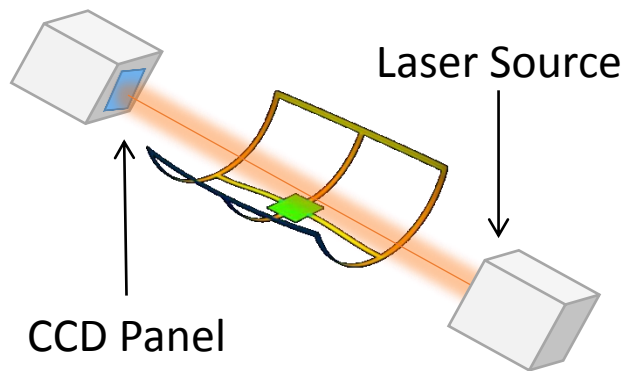


Figure 15 – Horizontal optical measurement

The second method would be to expose the surface to a perpendicular laser light. This method has been used in other work to monitor the deflection of cantilevers under temperature change by Rogers at Murray State. In this case, the output reflection has a 90 degree shift when the square symmetric structure changes state. The platinum surface will

act as strips of concave mirror surface, and the light response to this change would be clear. Figure 16 demonstrates the reflective profile of a device from above. When switched into the other state, this profile will be rotated 90 degrees. The mechanical motion of this system makes this interferometric measurement possible.

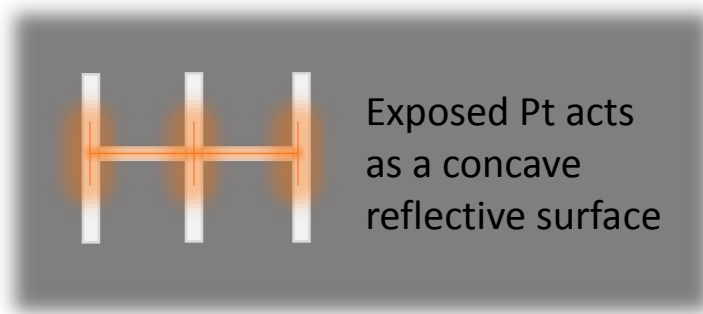


Figure 16 - Concave profile for vertical reflection

An optical method has some advantage in this system. It allows for a two dimensional array of structures to be read on a surface, as opposed to the parallel reading technique. This increased the amount of sensing elements per area that can be functional in a packaged device. These structures do not require an electrical connection to operate because their functionality is embedded in the geometry, so the only limitation is the beam focusing restrictions and resolution of the capturing CCD. Multiple devices would be captured at once, and a digital system could sort the signal into individual devices in post-processing. Issues with fabricating an electronic interface to the 3D structures are also eliminated.

The optical sensing technique has drawbacks to consider. The measuring system itself is more complex than simply measuring a capacitance or resistance, so this could increase the overall cost of the system. The optics will also require a larger setup and

possibly more complex computing to extract usable data from the CCD signal. The power required will depend on the measurement laser and required processing. Low-power LED and CCD array may make it feasible to perform this sensing on-chip. An optical sensing method is more feasible than electrical measurement for recording the state of an array of sensing structures.

2.3.3 Advantages of Autonomous Sensing

The proposed system would allow remote data collection. The bistable nature of the device provides an advantage over analog systems that must be read during a sensed event. An array of structures with a switching threshold (a critical temperature or vibration frequency, for example) would react to an event and retain that data physically. This allows for flexibility in the data recording approach and may give insight into situations where constant data collection is difficult.

For example, a packaged array that responds to a vibration magnitude could be attached to a soldier who is exposed to hazardous sound levels from gunshots and explosives. The threshold levels reached could be sensed off the battlefield later and the devices could be reset using nIR techniques being developed. These powerless threshold sensors may also be useful for space exploration, where radio connection is often interrupted and even small power consumption would be critical in a long term mission. Temperature data could be collected passively with threshold devices during logistically intense situations such as passing close to a celestial body or atmospheric entry.

CHAPTER III

AN OPTIMIZED POLYMER FILM WITH GOLD NANOPARTICLES

The proposed hybrid MEMS structures are reliant on understanding the power transfer physics behind driving the thermomechanics with light. This chapter presents the development, optical absorption, thermal properties of a thin-film platinum device coated with gold nanoparticles. These particles are engineered to have a light absorption peak near 808 nm. The response of bare and particle-coated thin-film platinum was examined under an 808 nm infrared laser. The results show that a particle coating is a significant factor in the thermal efficiency. This work is the foundation for wavelength-specific MEMS actuators powered by infrared light.

3.1 Developing a GNP Film

Biomedical engineering has benefitted greatly from advances in MEMS. Small-scale actuators and switches have potential in areas such as microscale pumping [98] and cell manipulation [99]. Powering these micro devices is often a challenge because of the invasive wiring needed. Tissue-permeant infrared (IR) light has been used in therapeutic applications [100], and provides a noninvasive energy transfer method for heating nanoparticles with enhanced IR absorption for cancer cell ablation [101]. Depositing these particles onto a MEMS device could provide new optically induced functionality if the absorption behavior remains the same.

The potential to use this heating method to provide thermal energy in MEMS applications has not been thoroughly investigated. However, many MEMS are thermally driven such as thermal expansion based actuators [102] and microfluidic pumping elements [46]. The most common MEMS heating mechanism is direct current (Joule) heating, but this requires wiring to the active region which is undesirable in biomedical applications. Coatings such as platinum black have produced absorbing layers for thermal infrared detectors [103] and inkjet printing has been used to localize absorption at the macro scale [104], but these layers are not wavelength-selective. Wavelength-matched air gaps work well to tune thermal absorbers, but the absorbance wavelength must be decided at the start of the process, and will be the same for all devices on a wafer [105]. An optically induced temperature gradient using wavelength-selective printable or spinnable coatings would provide a more versatile method of wireless and non-invasive thermal actuation. This project examines the particle and surface interaction that will be the focus of ongoing effort to develop novel biomedical applications for this technology.

Metal nanoparticles are one of the basic building blocks of nanotechnology. Gold nanoparticles (GNPs) have attracted enormous attention in chemistry, biomedicine, and electronics due to their very small size, oxide-free surfaces, bio-conjugation properties, good biocompatibility, and unique optical properties. Specifically, because of their optical activity in the near infrared (nIR), GNPs are extensively utilized in immunoassay [106, 107] and drug delivery systems [108] as well as imaging, detection [109], and thermal therapy for cancer [110].

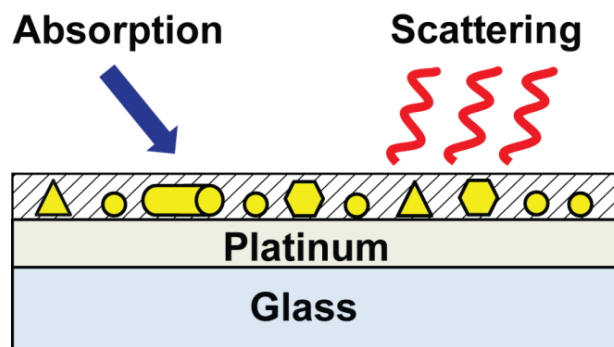


Figure 17 - This Figure shows an overview of the system being characterized in this work. Particles are coated onto a Pt trace on a glass substrate. Light at a certain wavelength is applied. Absorbed light will provide additional thermal energy to the system.

3.2 Plasmonic Heating Characterization

Each particle acts as a plasmonic heater. This property of the GNPs is based on a phenomenon called surface plasmon resonance. The mean free path in gold is around 50 nm [111]. Therefore most of the interaction in a gold nanoparticle is with the surface. Incoming light energy causes the electrons on the shell of the GNP to oscillate and a resonance condition can be reached if the wavelength is larger than the particle dimension. The migrating charge on the particle surface causes a changing electric field to induce heating. The absorption and electric field created are affected by the particle geometry [112]. The particle solution used in this report contains a mixture of particle shapes and is engineered to converge on the desired absorption properties.

For this work, the absorption of the particles when coated on a platinum layer is of interest. A metal surface is a typical feature in MEMS structures, and the particle interaction and thermal properties under laser light will be important in designing mechanical behavior. Figure 17 contains a schematic of the working principle. The platinum thin film serves as a resistive temperature sensor to measure the thermal properties. Selected areas of the MEMS structures will be heated and thermal gradients may even be created from a single light source by patterning the particle deposition.

3.2.1 Particle and Substrate Fabrication

A meandering thin-film platinum resistor was developed to monitor the behavior of deposited nanoparticles under near IR stimulation. This structure allows for accurate measuring of the surface temperature. The hybrid optothermal test structures are created by combining the resistor with the GNPs. Platinum is used as the surface layer because of its biocompatibility and functionality in high-displacement MEMS actuators [36].

Gold nanoparticles with precisely controlled near infrared (nIR) absorption were synthesized by one-step reaction of chloroauric acid and sodium thiosulfate, without assistance of additional templates, capping reagents or seeds assembly. The nIR absorption wavelengths and average particle size increase with increasing molar ratio of $\text{HAuCl}_4/\text{Na}_2\text{S}_2\text{O}_3$. This provides the base for synthesis of gold nanoparticles with tunable nIR absorption wavelength. The nanoparticles produced from this reaction include small spherical colloidal gold particles with resonance at 530 nm and anisotropic gold nanostructures with nIR resonance. The pseudo-spherical crystals have diameters in the range of 15 to 45 nm, and the edges of the nanoplates are in the range of 40 to 90 nm. The tunable peak range for the particles used is from 800 to 1100 nm [113]. Other work has shown that geometry selective processing can yield gold nanorod solutions that have a peak absorbance between 600 and 1000 nm [114].

The planar resistors were fabricated with a single mask cleanroom fabrication sequence. First, photoresist was deposited and patterned to define the metal features on the surface of a 500 μm thick borosilicate float glass wafer. A 200 nm layer of platinum was deposited by sputtering after a brief deposition of titanium to aid adhesion. The intended metal geometry was defined via liftoff of the photoresist. After drying, the planar resistor is complete and can be coated with nanoparticles.

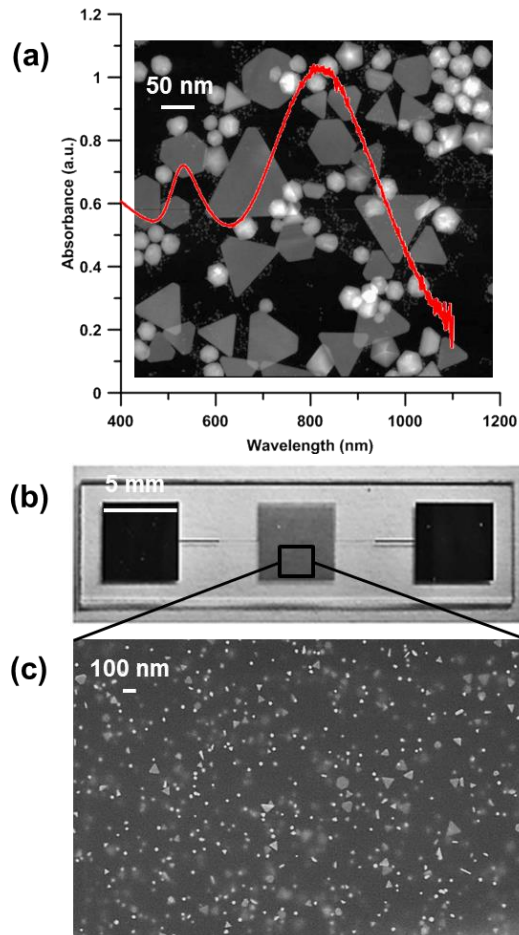


Figure 18 - (a) Optical absorption spectrum of synthesized gold nanoparticles, with a TEM image of particles as background. (b) Fabricated planar resistor used to gather temperature measurements. (c) SEM images of GNPs with PVP polymer matrix after spin-coating on the platinum test surface.

The spectrum of the GNPs used for this experiment is shown in Figure 18 (a), and the absorption peaks of each type of GNP are clearly seen. The particles are coated onto the center square in Figure 18 (b). This region contains a long (0.58 meter) thin-film resistor trace with a 20 μm width and 200 nm thickness that zigzags to fit within a 5mm square. The left and right solid blocks are bonding pads for interfacing with the test surface. SEM

images were taken after GNPs were distributed on the surface. The particle distribution on the platinum surface can be seen in Figure 18 (c). Samples were prepared by spin-on deposition of gold nanoparticle solutions with optical density (OD) of 100 onto an air plasma treated surface. The OD is a measure of the particle concentration in a fluid medium.

3.2.2 Nanoparticle Dispersion

The nIR resonant GNPs were found to most evenly disperse with spin-on coating at 4000 rpm at a somewhat uniform thickness. However, if the particles were in a water medium, the adhesion was not sufficient for any of the substance to remain on the surface and coat the device when the spinning was applied. The polymer polyvinylpyrrolidone (PVP) has been used in other work as a suspension for nanoparticles [115], and was included in the liquid medium at 8% concentration to act as a matrix for the particles on the surface. This allowed for a uniform film to remain across the test resistor. The average film thickness was measured to be approximately 150 to 200 nm. A PVP film without GNPs was shown to have the same thermal behavior as a bare surface to ensure the GNPs are the active heating element.

The GNP film was created using a suspension with an optical density (OD) of 100. Films were created from OD ranging from 25 to 200 to determine an optimum spread. High OD films often showed particles aggregating together. This behavior will interrupt the plasmonic heating properties and lower the heat generation efficiency. However, a higher dispersed particle count will add to the heat generation. Minimal particle aggregation was observed with the 100 OD film, and SEM analysis showed that the GNPs

were distributed normally on the surface with a mean density $\mu = 50$ particles per μm^2 and standard deviation $\sigma = 13$.

3.3 Characterization Objectives

The first objective of this work is to verify that a thin-film polymer film with suspended gold nanoparticles will provide enhanced nIR absorption. A batch of 20 samples was made to contain half bare and half particle coated surfaces. The two sets were exposed to a fixed nIR light intensity for a defined trial period. The surface temperature during the heating and subsequent cool down was recorded and the resulting curve was analyzed for maximum temperature and other properties related to thermal efficiency, such as a thermal time constant.

Quantifying the absorption effect is critical for the design of future devices. The experiment was repeated with multiple devices from different wafers. This allowed us to determine if there was a wafer-to-wafer effect in the device operation and strengthened the significance of the data collected during the trials by repeated measurements.

This fabricated device was also used for a second experiment. A study of the surface response to varied laser intensity was performed. Previous theoretical work on single gold nanoparticles predicts a linear temperature response to energy input [116]. However, the heating profile of a particle film on a metal surface has not been previously confirmed.

The diode laser energy intensity on the surface was adjusted by changing the height of the focusing lens from the surface, and the energy per area is easily calculated and measured by recording the spot size. The metric used for this analysis is the maximum temperature reached by the substrate after two minutes.

These two metrics combined provided valuable insight into effectiveness of coating a surface with GNPs to enhance absorption. The magnitude of the thermal response is critical in designing future devices to operate on the nIR absorption principle. The behavior

change with laser intensity will make it possible to tune the heating amount as needed. This will be of paramount importance for biological applications, where a thermal limit for living tissue will be a factor.

3.3.1 Experimental Setup

The tools needed to characterize the surface include a laser source, amplifying circuit, and LabVIEW interface for data collection. Figure 19 shows a schematic of the setup. The LabVIEW console controls the laser and receives the output from the amplifier circuit with a USB - 6009 data acquisition unit. The laser beam focusing head is suspended above the sample stage.

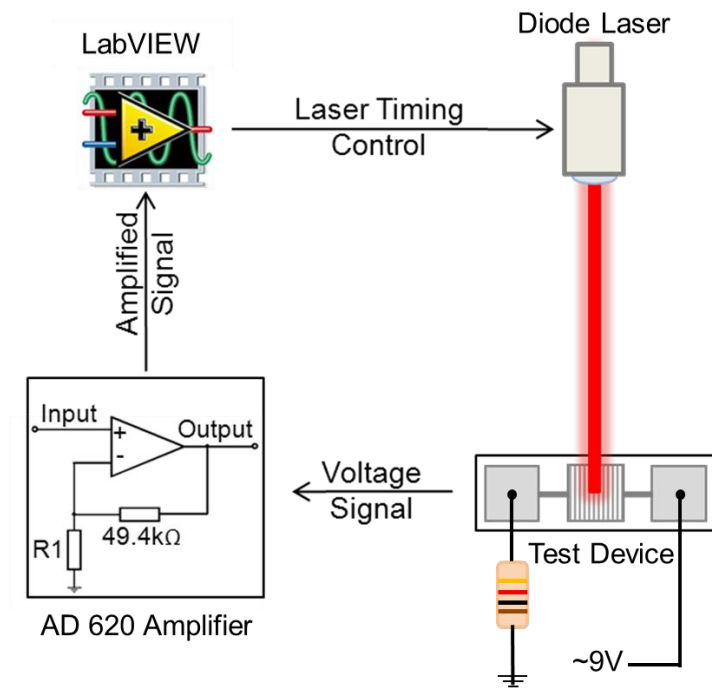


Figure 19 - Thermal efficiency measurement setup: a LabVIEW console operates the 808 nm laser, and resistance-induced temperature changes are calculated from voltages measured by an amplifier circuit.

Surface particles are excited by a 5 W diode laser (808 nm). The intensity of the laser for the first experiment is 1.433 W/m² and the initial temperature is 22°C. The voltage across the fabricated resistor is extracted from a voltage divider setup and is conditioned by an AD620 amplifier with 50x (adjustable) gain. The expected analog value being read by the software is estimated by Equation 6. The temperature can be observed by measuring the electrical resistance of the metal trace, which follows Equation 6. The amplified output is read by a NI USB-6009 data acquisition unit and collected in LabVIEW software.

$$V_0 = GV_S(R_1/(R + R_1)) \text{ Equation 6}$$

The expected voltage output (V_0) is a function of the amplifier gain (G), the source voltage ($V_S=9$ V), the fixed resistor ($R_1=1000$ Ω) and the sample resistance (R). The temperature change corresponds to the resistance-temperature relation in Equation 7.

$$\Delta R = R_0(\alpha\Delta T) \text{ Equation 7}$$

The resistance change (ΔR) is defined by the initial value (R_0) and change in temperature (ΔT). The thermal coefficient of resistance (α) is a material constant. In a metal, the resistance will increase with applied thermal energy due to increased electron collision with the lattice structure.

The thermal coefficient of resistance (α) of thin-film Pt is known be less than the bulk value (0.0039°C⁻¹). The resistors in this work were measured to have $\alpha \approx 0.0013$ °C⁻¹) by monitoring resistance while applying a known temperature increase of 100°C to the structure. The coefficient was determined by the relation shown in Equation 7. The calculated value is in the range of past studies examining sputtered thin-film platinum [117, 118]. This device is best used below 300°C because the thin-film will show the effect of strain from thermal expansion in the resistance at high temperature.

The software manages the laser operation and trial times as defined by the user. Standard run time for this experiment is four minutes total. The laser is activated for two minutes, followed by two minutes of device cool down. The data being collected at is packaged into an array at two Hz and written to a text file for further analysis. The time, recorded analog voltage, and calculated resistance are recorded in respective columns.

3.4 Particle Effect on Surface Heating

The data indicates that a platinum surface coated with functionalized GNPs absorbs more incoming light than a bare surface. The average temperature difference was observed to be about 15 degrees Celsius between the surface types, as seen in Figure 20. The spread of the data is due to inconsistencies in the dispersion of the deposited particles and is illustrated in Figure 21. Applying a general analysis of variance (ANOVA) model to the data shows that particle presence on the surface is a significant factor in the max sample temperature with a 95% confidence interval ($R^2=0.87$).

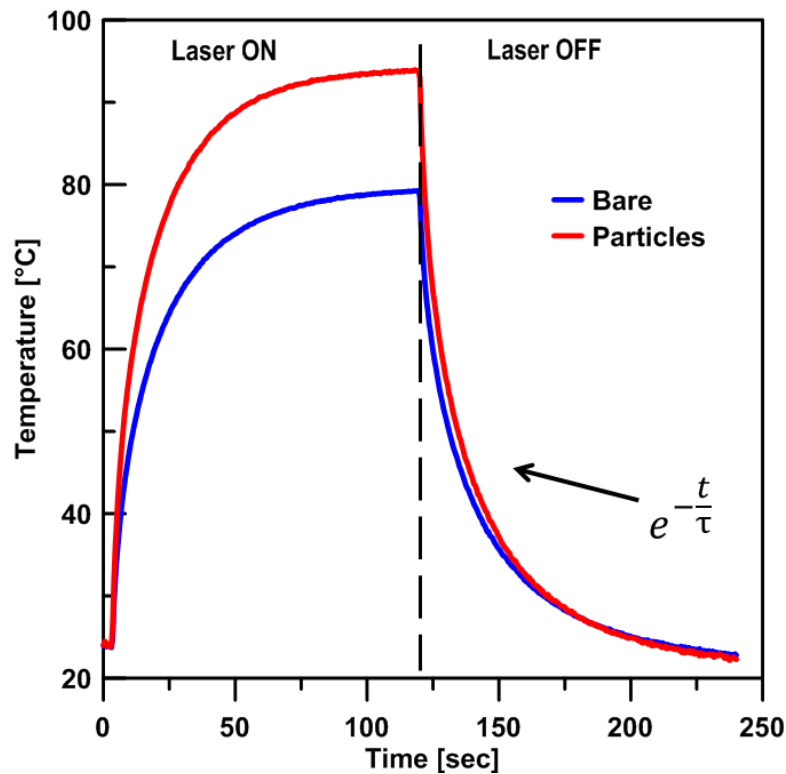


Figure 20 - Temperature data is averaged from each sample set. The time constant was calculated from the exponential cool down from 120 to 240 seconds and the decay equation is shown in the Figure.

This energy difference is sufficient to create a temperature gradient in a MEMS device. The spread of the peak temperature data is displayed in more detail in Figure 21. The right box represents the sample set that was coated with GNPs. The spread of the samples for each set can also be attributed to imperfections in the fabricating and seating of the device on the test platform. A non-uniform contact to the surface would affect the thermal transfer into the bulk below the device.

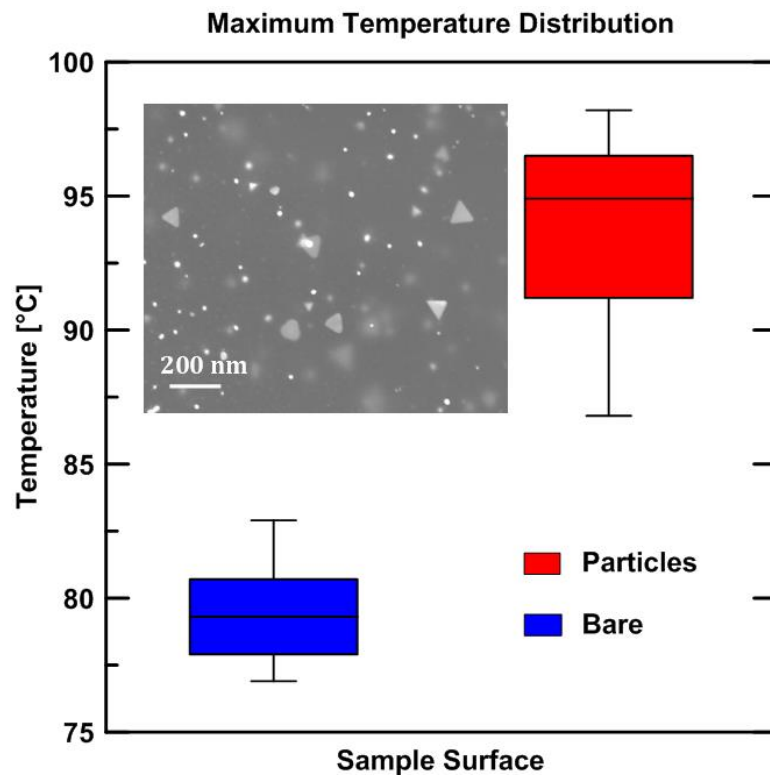


Figure 21 - The box plot of the data demonstrates the difference in optical absorption when nanoparticles are applied to the surface.

The most influential factor in the spread of the data is the distribution of the GNPs on the surface of the device. Outliers in the data can be correlated to films that do not have uniform deposition under optical inspection. The test cycle was repeated on each device

three times, and the film response was consistent over this time. Devices that were exposed to the laser for longer amounts of time reached an asymptote after three minutes and remained in energy balance between the input laser energy and heat sink effect of the surroundings without degradation of the particle film's effect.

Particles can be selectively applied to regions of a surface. A method for selectively spin-coating nanoparticles has been adapted for this project. A stencil is created on the wafer surface by patterning Parylene-C. This method has been used in many applications [119, 120]. The polymer is deposited and then masked with standard photolithography. The stencil features are created by plasma etching through openings in the SPR 220 photoresist. After spin-coating particles, the Parylene-C is peeled away, leaving only the particles deposited through the pattern.

3.4.1 Thermal Efficiency

The thermal efficiency of the surface is also of interest in this investigation. This measure lets the optical performance in this work be compared to other similar systems, and is a key metric in thermal solar absorbers. The information within the preceding Figures can be used to give insight into the response of the system to laser light. An estimation of the thermal efficiency can be derived from basic thermodynamics theory and the known material and geometric properties of the samples.

The derivation is performed with the goal of producing a ratio of total thermal energy in the system Q over the energy input from the laser source. The assumptions for this calculation are that the laser intensity is uniform, that the thin-film Pt holds a small fraction of the thermal energy and most of the storage is in the substrate, and that the bottom

of the device is thermally grounded. The thermal efficiency (η) is calculated in Equation 8 as follows:

$$\eta = (\Delta T c_v d) / 2\tau I \text{ Equation 8}$$

The ΔT is represented by the difference in the maximum and minimum temperatures measured ($T_{\max} - T_{\min}$). This is multiplied by volumetric heat capacity (c_v) and thickness (d) of the substrate. The intensity of the laser in this system (I) and the time constant (τ) are also factors. The maximum temperature and cool down time for this calculation are pulled from this sample average data in Figure 21. The calculated factors for the bare and coated substrates are summarized in Table 1.

Factor	Bare	Coated
Time Constant (τ)	24.4738	18.4775
Max Temp (C)	77.8	94.8
Efficiency (η)	0.0685	0.1193

Table 1 - Thermal Efficiency of the Particle-Coated and Bare Surfaces

The particle coated surface shows about 75% greater thermal efficiency compared to the bare platinum. Applying the particle film increases the thermal efficiency of the device from 6.85% to 11.93% on average. In these test structures, the temperature exceeds physiological limits for living cells. However, changes in the light intensity, device

geometry, and materials would result in devices that are suitable for use in biological systems.

3.4.2 Response to Varied Intensity

Adjusting the maximum temperature has also been addressed in this study. Each GNP acts as a plasmonic heater, and is predicted to have a linear response to light intensity. Trials were performed at a range of intensity levels to confirm this property, and the results are shown in Figure 22. It is clear from the data that the response of the surface heating is linear. A regression was calculated with a linear model, and it was found to fit with an R-squared of 0.9998, indicating that this is an appropriate model for the system.

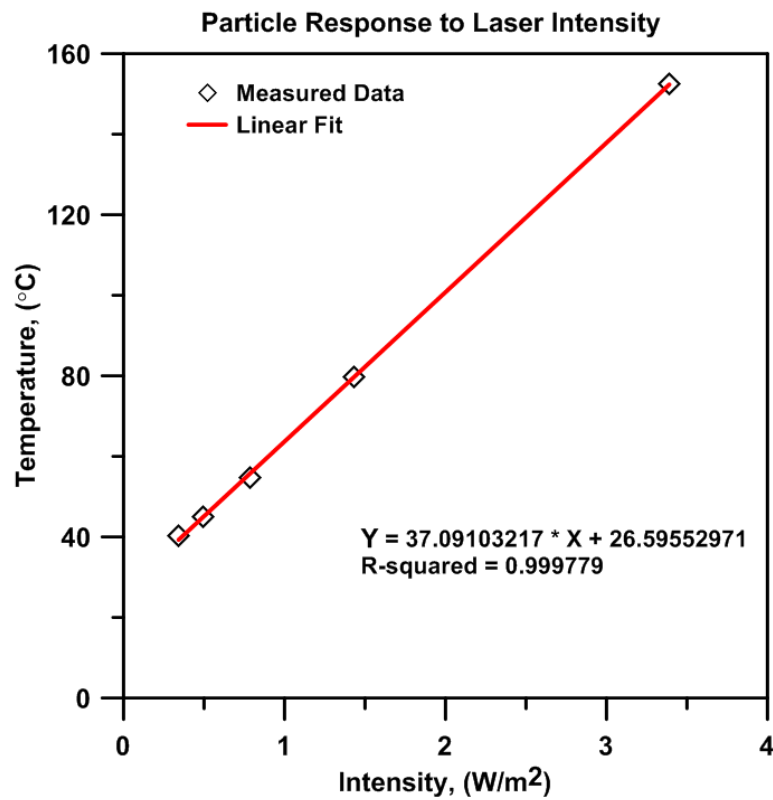


Figure 22 - The intensity levels correspond linearly to temperature.

A predictable response is a valuable feature of this particle film for two primary reasons. First, in future applications of this method, a known model to apply to the heating behavior will make it easier to define proper device operating conditions. Many biological systems are very temperature sensitive, and modeling the response to possible input will be a high priority. Second, this lends some credibility to the assertion that the particles dispersed on a surface act the same as they do when modeled individually or are floating in a liquid medium. The integration of MEMS requires that the behavior is characterized for on-chip situations.

5 Conclusions on Single Wavelength Tuned Film

Optical stimulation was used to induce surface heating of a GNP-coated platinum surface. The heating performance of the surface was monitored to show the effect of depositing near IR absorbent particles on the surface. A significant increase in optical absorption at 808 nm wavelength was verified. The thermal efficiency was calculated and can be used for comparison with other thermally and optically driven MEMS techniques. Linear response to varied light intensity was also confirmed.

This hybrid of infrared absorbent gold nanoparticles and MEMS fabrication technology has potential applications in light-actuated switches and other mechanical structures. Deposition methods and surface chemistry are being integrated with three-dimensional MEMS devices in the next phase of this work, where a bistable MEMS structure has been developed to make use of this heating principle. Selective thermal expansion powered by an infrared laser is localized at critical regions that are coated with infrared-resonant gold nanoparticles. Actuation at laser power and thermal limits compatible with physiological applications will enable microfluidic pumping elements, studies of tissue response to three-dimensional mechanical stimuli, and other devices triggered by tissue-permeant infrared light. The long-term goal of this project is a system of light-powered microactuators for exploring cells' response to mechanical stimuli. Such devices could apply forces at the cellular scale, offering potential therapies for heart disease and osteoporosis, and increasing our fundamental understanding of tissue response to everyday mechanical stresses at the molecular level.

CHAPTER IV

PARTICLE FILMS AT TWO WAVELENGTHS

This chapter demonstrates a basis for designing light-powered MEMS with a wavelength specific response. This is accomplished by patterning surface regions with a thin film containing gold nanoparticles that are tuned to have an absorption peak at a particular wavelength. The heating behavior of these patterned surfaces is selected by the wavelength of laser directed at the sample. This method also eliminates the need for wires to power a device. The results demonstrate that gold nanoparticle films are effective wavelength-selective absorbers.

4.1 Wavelength-Tuned Particles

Development of microscale actuating technologies has been critical for interacting with natural components at the cellular level [121, 122]. Actuation, driven by differential thermal expansion, has been used to create large deflections with high force relative to electrostatically driven systems [102, 123, 124]. However, many thermally based techniques require a physical connection for power and operate outside the temperature range conducive for biological studies and medical applications. Stimulating devices with laser light offers a versatile wireless medium for powering and controlling a microscale element. This work demonstrates the basis for designing light-powered MEMS with wavelength specific response.

This project builds on recent developments in gold nanoparticles (GNPs) that resonate within the 650-1050 nm biological “optical window” where tissue is not strongly absorbent [125]. In the previous investigation, a thin-film polymer with suspended GNPs increased near infrared (nIR) absorption compared to a nanoparticle-free surface at a single wavelength [126]. This chapter discusses surface heating trials with two different wavelengths, 808 nm and 915 nm, of tuned GNPs in order to characterize and compare the heating of wavelength matched and non-matched GNPs.

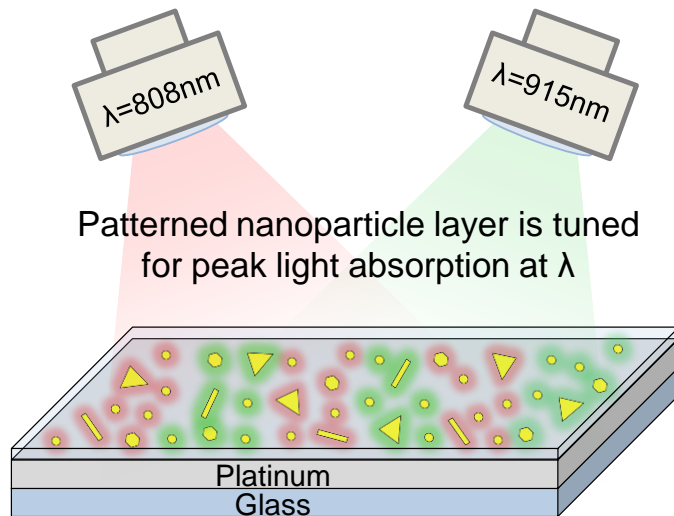


Figure 23- A concept drawing of a patterned gold nanoparticle film that will show a different response to a particular wavelength. Patterned areas may heat more strongly in response to a specific wavelength of light.

4.1.1 Synthesizing Gold Nanoparticles

A meandering thin-film platinum resistor is developed to monitor the behavior of deposited nanoparticles under near IR stimulation. The hybrid optothermal test structures are created by coating the resistor with the GNP film. Platinum is used as the surface layer because of its biocompatibility, functionality in high-displacement MEMS actuators, and resistance change when heated [36].

Gold nanoparticles with precisely controlled near infrared (nIR) absorption are synthesized by one-step reaction of chloroauric acid and sodium thiosulfate in the presence of a cellulose membrane. The nIR absorption wavelengths and average particle size increase with increasing molar ratio of $\text{HAuCl}_4/\text{Na}_2\text{S}_2\text{O}_3$. The gold salt used is hydrogen tetrachloroaurate (III) trihydrate 99.99% ($\text{HAuCl}_4 \cdot 3\text{H}_2\text{O}$) purchased from Alfa Aesar. A 1.72 mM solution is prepared with DI water and protected from light with aluminum foil.

A 32.6 ml volume of the 1.72 mM gold salt solution is combined with 7.4 ml of a 3 mM sodium thiosulfate pentahydrate solution ($\text{Na}_2\text{S}_2\text{O}_3 \cdot 5\text{H}_2\text{O}$; purchased from Sigma-Aldrich) to perform the reactions for synthesizing the nIR GNPs (808 nm at this ratio).

A 12 kDa MWCO membrane (Flat Width = 43 mm) from Sigma-Aldrich is cut to the desired length (150 mm for 770 nm GNPs and 100 mm for 940 nm GNPs), then one end of the tube is closed with a weighted dialysis clip and filled with the gold salt solution. The $\text{Na}_2\text{S}_2\text{O}_3$ solution is then added into the tube via pipette followed by mixing of the solution within the membrane by manually stirring with the tip of the pipette and aspirating with the pipette pump. Subsequently, air is removed from the tubing and the other end of the membrane is clipped. The sealed tube is placed in an 8 L beaker filled with 7 L of DI water with a stir bar at the bottom of the beaker rotating at 200 RPM and allowed to react for 1 hour. Particle batches, composed of various pseudo-spheres and anisotropic nanostructures [113], are dispersed in 8% PVP by weight solution to make the polymer GNP mixture used for this experiment with the spectra seen in Figure 24.

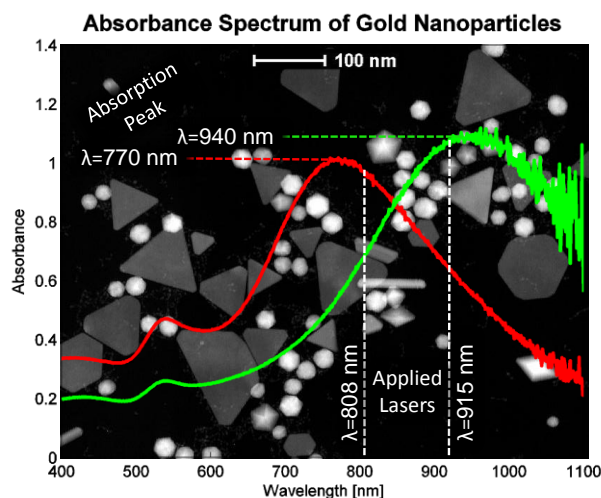


Figure 24 - The absorbance spectrum of the two batches of GNPs used for this experiment.

The planar resistors were fabricated with a single mask cleanroom fabrication sequence. First, photoresist was deposited and patterned to define the metal features on the surface of a 500 μm thick borosilicate float glass wafer. A 200 nm layer of platinum was deposited by sputtering after a brief deposition of titanium to aid adhesion. The serpentine metal trace in a 0.5 cm square was defined via liftoff of the photoresist.

4.1.2 Film Deposition

Spin coating is used to disperse the polyvinylpyrrolidone (PVP) GNP solution on the substrates. A pipette is used to place a 35 μL droplet on the center of a device, and then the solution is dispersed by spinning at 4000 rpm for 10 seconds. The device is then baked on a 115°C hotplate for 2 minutes to stabilize the film. Typical thickness of a PVP GNP film is approximately 100 μm . At this thickness, not all particles are flat on the surface and may be at varying height and orientation, as observed in Figure 25.

In previous experiments, nanoparticles suspended in PVP solution were patterned by spinning the solution on wafers through a peelable polymer stencil [119], as the final step before the devices are released from the substrate. The stencils can be patterned in registration with microfeatures already on the wafer. Spun-on PVP-dispersed nanoplate films remain plasmonically active with a stable peak absorbance as long as the concentration of particles in the solution is not too dense, ≤ 50 nm between GNPs, to avoid shifting the resonance peak due to the particles interfering with each other in the dried film [127]. In preliminary work, polymer removal did not pull off previously-deposited nanoplate coatings, suggesting that it may be possible to pattern a second layer. A SEM image of a 100 OD GNP film with 8% PVP can be seen in Figure 25. For this work, devices

are simply masked over the bonding pads and exposed over the entire central temperature sensing region.

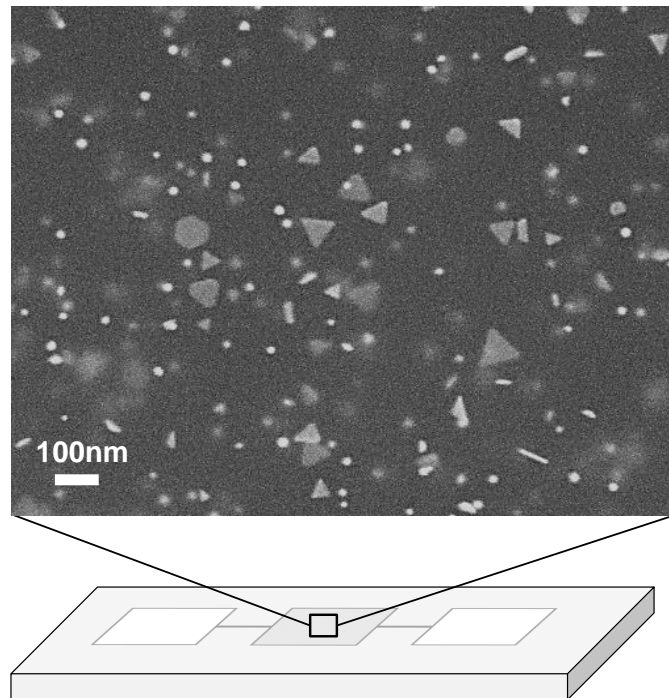


Figure 25 - Drawing of the test thermometer surface used for this work and a SEM image of a GNP film.

4.2 Experiment Setup

This experiment is performed with a two-laser setup. Surface particles are excited by a 4 W diode laser for two-minute intervals; first the 808 nm laser is activated for two minutes, followed by a two-minute cool down, and then the 915 nm laser for two minutes and a corresponding two-minute cool down. The voltage across the fabricated resistor is extracted from a voltage divider setup and is conditioned by an AD620 amplifier with 50x (adjustable) gain. The resistance change corresponds to the resistance-temperature relation in Equation 7. A schematic of the setup used is seen in Figure 26.

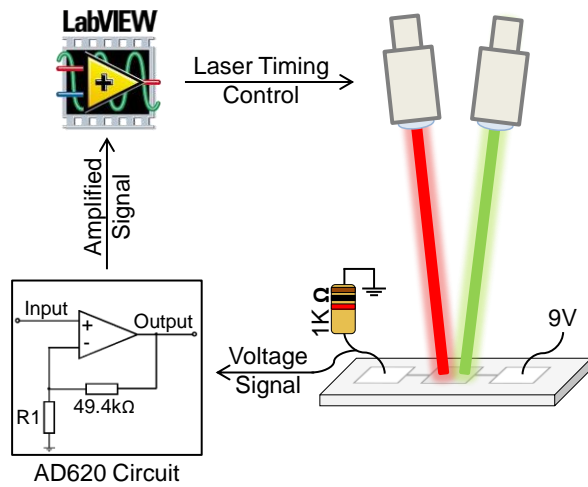


Figure 26 - Experimental Setup with Two Laser Sources.

The sample set used for this experiment consists of three sets of five devices. The first is a set of bare resistors to provide a base level heating comparison. The absorbance spectrum of an 8% PVP film without GNPs is measured to demonstrate that a PVP film without GNPs does not add to the absorption spectra. Next, five surfaces with a film of 707 nm GNPs and five surfaces with 940 nm GNPs were created. Trials with both laser

wavelengths are performed across all devices. The data is averaged for each wavelength set and plotted on the same axis for comparison.

3 Interpreting the Surface Performance

The data is transformed into temperature data through the relation in Equation 7 and is plotted against time in Figure 27 (A) and (B). The time sequence has been separated into two portions, where (A) represents the trial time for the 808 nm laser, and (B) represents the cycle with the 915 nm laser. The two are collected consecutively, but the overall 8 minute timing sequence has been divided between Figure 27 (A) and (B) to more clearly illustrate the effect of each laser. The blue trace represents the bare sample in each plot. The red and green traces show the response of the 770 nm and 940 nm GNPs.

The plots shows that the type of film deposited on a surface will determine the heating profile. In each case, it is seen that the GNP film with the highest absorption will heat the most under a specific laser source. Figure 5 (A) shows the trials with the 808 nm laser, and as expected the 770 nm GNP film performed the best. The same idea is expressed in (B), where the 940 nm GNP film was most responsive to the 915 nm laser. The particles still show enhanced absorption in both cases, although the energy difference between the films is not as large as either wavelength-matched film to the bare surface. This predictable energy difference is further evidenced by the small standard deviation of each data set, which is displayed in the lower-left of the plot in (A) and (B).

Figure 27 (C) shows the net percent change that each particle showed compared to the bare surface. This measure was chosen to normalize the data against the heating of a bare surface. Thereby, yielding a comparable metric between the laser wavelengths applied, which excludes influences from the absorption of platinum and differences in the focal spots of the two lasers. The wavelength selective nature of the two GNP films is

clearly seen in this format. This is important for demonstrating that a difference can be obtained by patterning a particle film, which was the goal of this work.

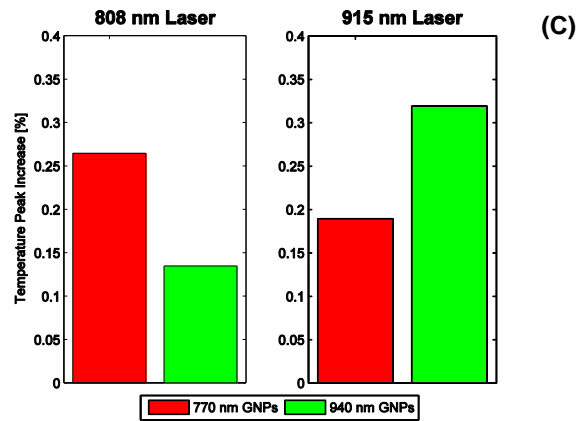
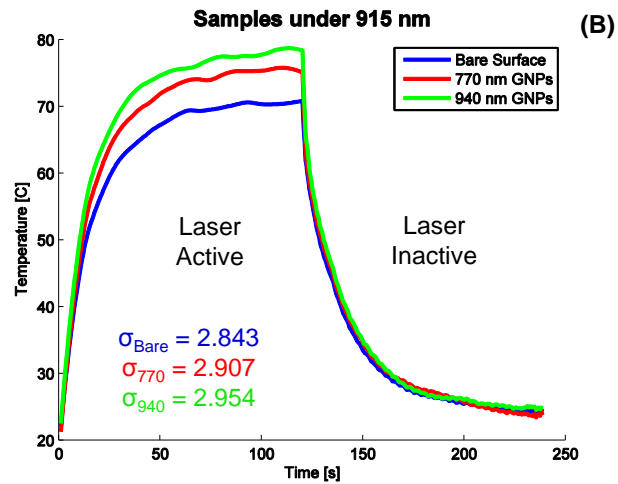
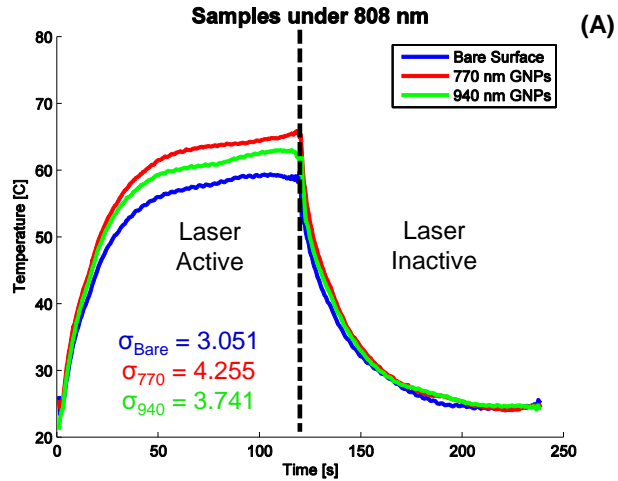


Figure 27 - Temperature increase vs. Time for GNP-coated and control surfaces illuminated by A) 808 nm and B) 915 nm laser light. (C) A normalized comparison of the temperature increase of each film type (y-axis unit is % / 100).

The 770 nm and 940 nm peak solutions were diluted to have an OD of 25 and 100, respectively. The OD is a measure of absorbance of a solution. The two solutions are diluted to different levels to more clearly demonstrate the difference in peak absorption between the samples. At the same OD, the 770nm peak particles showed greater heating performance under either applied laser wavelength, although with a smaller gain at the non-optimum peak. By adjusting the OD, it was possible to achieve the temperature difference reversal shown in the results in Figure 27.

The data clearly shows an increased response to the optimum wavelength by the particle films, displayed in red and green. The bare surface, shown in blue in Figure 27 (A) and (B), is less responsive to all light, as expected. However the substrate does have some absorption at these wavelengths, evidenced by the heating that occurs. Higher selectivity could be achieved by using a non-infrared absorbing temperature sensitive surface. In that case, the only IR-absorbing part of the device would be the nanoparticles, so differential thermal expansion could occur at lower laser doses.

4.4 Possible Optimizations

A future goal is to move the red and green traces farther apart in Figure 27 by narrowing the absorption peak of the film through a combination of more uniform synthesis conditions and better size separation techniques, aiming for a ~ 10 °C difference or greater. Alternatively, there are many commercially available gold nanorods and other anisotropic gold or silver nanoparticles with sharp absorption peaks that increase selectivity of the response [101, 128-130]. Also, adjusting the maximum temperature is critical for biomedical applications, where these films would need to operate at relatively low temperatures (<40 °C) and laser power (<1.2 kJ/cm² [131, 132] at wavelengths that tissue is relatively transmissive) for biocompatibility. The temperature sensitivity can be controlled by adjusting the laser power targeted at the device since particle heating is linear with respect to the energy input [116].

Coatings described in this work could actuate MEMS/NEMS under illumination, even achieving fast cyclic actuation if different narrow-band wavelength selective coatings are patterned on different parts of the device. Discoveries in this work will feed forward to new applications in implanted photo-actuated mechanical devices. Because infrared light can pass through tissue, these devices could potentially trigger cardiac muscle or other cells that depend on an orderly mechanical impulse —without any batteries or wires inside the body. The future goals of this work include development of freestanding cyclic microactuators that can interact with cardiac, bone, and muscle cells, powered and controlled by tissue-permeable infrared light.

CHAPTER V

ENHANCING LIGHT-INDUCED THERMAL ACTUATION

The previous discussion has shown that the addition of gold nanoparticles to a solid surface will add a wavelength specific plasmonic heating element to the underlying material. This chapter advances that idea from a surface-deposited film to a layer on a microstructure that is out of the plane of the substrate. This new geometry is critical to investigate because of the dramatic difference in thermal mass between a solid substrate and a suspended element with a small footprint.

5.1 Combining Gold Nanoparticles with Pop-Up Structures

Bioengineering has benefitted greatly from advances in MEMS. Small-scale actuators and switches have potential in areas such as microscale pumping and cell manipulation. Powering these micro devices is often a challenge because of the invasive wiring needed. Tissue-permeant infrared (IR) light has been used in therapeutic applications [100, 114] and provides a noninvasive energy transfer method for heating gold nanoparticles (GNP) with enhanced IR absorption for cancer cell ablation. Depositing these particles onto a MEMS device could provide new optically induced functionality if the absorption behavior remains the same.

The ability to use GNP-aided optical absorption to provide thermal energy for pop-up structures has not been previously investigated. The most common MEMS heating mechanism is direct current (Joule) heating, but this requires wiring to the active region which is undesirable in biomedical applications. An optically induced temperature gradient using wavelength-selective printable or spinnable coatings would provide a versatile method of wireless and non-invasive thermal actuation. This project aims to provide fundamental understanding of the particle and surface interaction that is required for developing new research avenues towards bioengineering applications.

For this article, the pop-up structure is fabricated from a patterned metal-oxide bilayer. The material strain is created during fabrication and is heavily temperature dependent. As the temperature increases, the material strain is reduced and the curved structure will lie flat in the plane. In contrast to thermal actuating principles that require wired conductive components for joule heating, the devices shown here are wirelessly

powered by near IR light by patterning a wavelength-specific absorbent gold nanoparticle (GNP) film onto the microstructure.

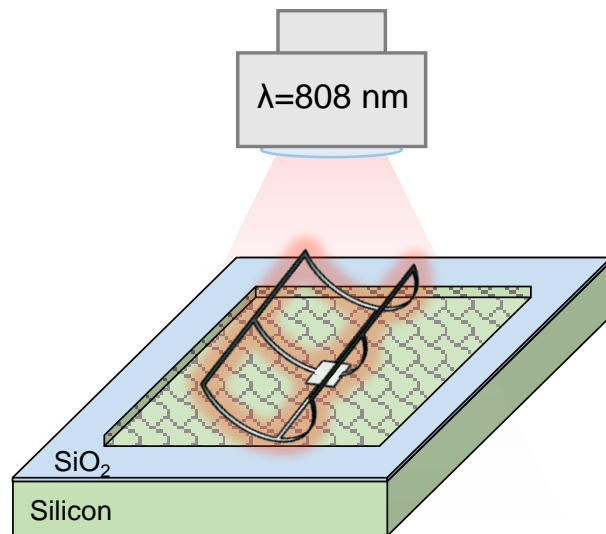


Figure 28 - Illustration of the system being investigated in this experiment.

The previous investigations showed that a polymer film with suspended gold nanoparticles will provide enhanced nIR absorption compared to a bare platinum surface at a single wavelength [126]. A following study presented surface heating trials with two wavelengths (808nm and 915nm) of tuned GNPs in order to characterize and compare the heating of matching wavelength GNPs, non-matched GNPs, and bare platinum surfaces [133]. The work presented here integrates this heating technology with thermally actuated pop-up MEMS structures, leading to the possibility of wirelessly applying a mechanical stimulus at the cellular level.

5.2 Fabrication

Composite structures with bistable geometry are the mechanical basis for this work. Strain between layers of SiO₂ and platinum is responsible for the out-of-plane feature and rapid temperature response [36]. Wavelength tuned GNPs are integrated into a polymer film and applied during the fabrication.

5.2.1 Gold Nanoparticle Synthesis

Gold nanoparticles with precisely controlled near infrared (nIR) absorption are synthesized by one-step reaction of chloroauric acid and sodium thiosulfate in the presence of a cellulose membrane. The nIR absorption wavelengths and average particle size increase with increasing molar ratio of HAuCl₄/Na₂S₂O₃. The gold salt used is hydrogen tetrachloroaurate (III) trihydrate 99.99% (HAuCl₄*3H₂O) purchased from Alfa Aesar. A 1.72 mM solution is prepared with DI water and protected from light with aluminum foil. A 32.6 ml volume of the 1.72 mM gold salt solution is combined with 7.4 ml of a 3 mM sodium thiosulfate pentahydrate solution (Na₂S₂O₃*5H₂O; purchased from Sigma-Aldrich) to perform the reactions for synthesizing the nIR GNPs.

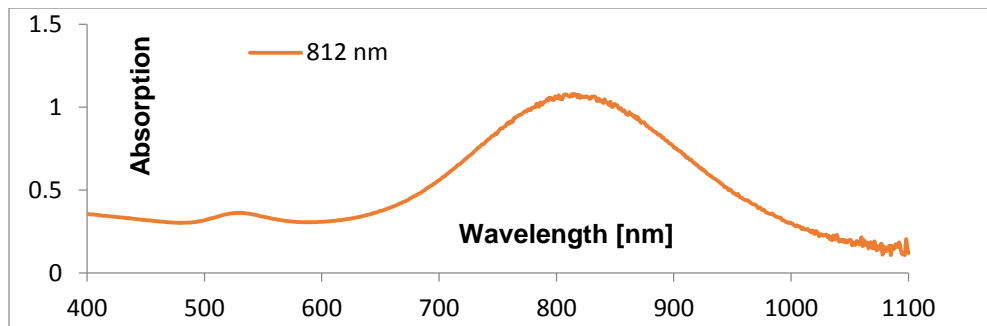


Figure 29 - Absorbance spectrum of the gold nanoparticles synthesized for this study with a peak at 812 nm, normalized by the spectrometer to a max y-value (absorbance) of 1.2.

A 12 kDa MWCO membrane (Flat Width = 43 mm) from Sigma-Aldrich is cut to the desired length (150 mm for 812 nm GNPs) then one end of the tube is closed with a weighted dialysis clip and filled with the gold salt solution. The $\text{Na}_2\text{S}_2\text{O}_3$ solution is then added into the tube via pipette followed by mixing of the solution within the membrane by manually stirring with the tip of the pipette and aspirating with the pipette pump. Subsequently, air is removed from the tubing and the other end of the membrane is clipped. The sealed tube is placed in an 8 L beaker filled with 7 L of DI water with a stir bar at the bottom of the beaker rotating at 200 RPM and allowed to react for 1 hour. Particle batches, composed of various pseudo-spheres and anisotropic nanostructures [113], are dispersed in 8% PVP by weight solution to make the polymer GNP mixture used for this experiment with the spectra seen in Figure 29.

5.2.2 Cleanroom Processing

The devices for this project are fabricated with a two mask cleanroom process. A standard 4 inch silicon wafer acts as the substrate for material deposition. The bilayer required for creating the pop-up geometry is created by first thermally growing a 500nm SiO_2 layer on the substrate. Photoresist is then deposited and patterned to mask the surface for the metal deposition. Next, a 10 nm/90 nm titanium/platinum (Ti/Pt) layer is deposited by sputtering, the features are defined by lift-off of the previous patterned photoresist. A second photomask is used to define where the SiO_2 will be etched to make windows to the silicon. The exposed photoresist and patterned metal act to mask areas of the SiO_2 while the wafer is exposed to a reactive ion etch to create open windows to the substrate. Before releasing the devices, spin coating is used to disperse the polyvinylpyrrolidone (PVP) GNP solution on the substrates. A pipette is used to place a 35 μL droplet on the center of a

device, and then the solution is dispersed by spinning at 4000 rpm for 10 seconds. The device is then baked on a 115°C hotplate for 2 minutes to stabilize the film. Typical thickness of a PVP GNP film is approximately 100 nm.

With evenly distributed particles on the surface, some of the residual PVP must be removed to allow the final release step. The devices are placed in a very low percent oxygen plasma for 30 seconds to remove the residual film that would otherwise prevent the Si substrate from being exposed to the etching gas. Finally, the previously etched oxide openings allow an isotropic XeF₂ etch of the silicon that is not hindered by the PVP film, and that releases the strained bilayer from the surface.

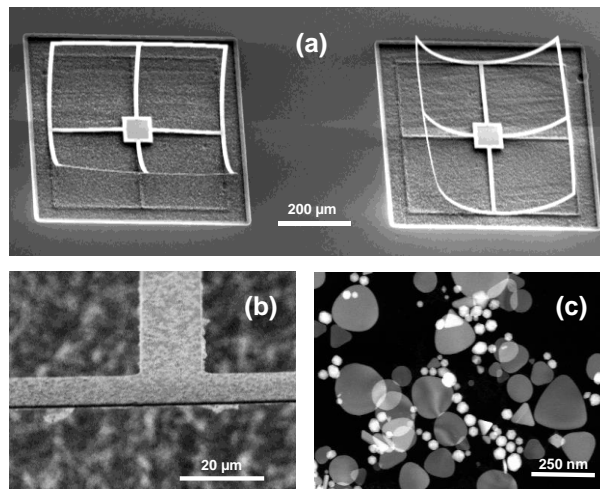


Figure 30 - SEM image of the fabricated devices (a), closer view to show the deposited GNPs (b), and a TEM of the gold nanoparticles (c).

5.3 Experiment Setup

An experiment was designed to characterize variation in the mechanical response of a popped-up microstructure when resonant GNPs are applied to the surface. When exposed to a specific wavelength of light, each particle acts as a plasmonic heater. This property of the GNPs is based on a phenomenon called surface plasmon resonance. The absorption and electric field created are affected by the particle geometry which allows the film to be tuned to add to the absorption of the substrate in a specific way, such as the 812 nm resonant GNPs used here.

5.3.1 Laser Control and Device Monitoring

The GNPs were tuned to this wavelength to match the available 808 nm diode laser. A schematic of the experimental setup is shown in Figure 31. The laser is controlled by a 490 Hz pulse width modulated (PWM) signal (5 watt at 100% power), generated by an Arduino Duemilanove with an ATmega328P microcontroller (a). The duty cycle (DC) of the waveform is varied to adjust the laser power (b).

The form of the surface structure while under the laser is monitored in an Olympus microscope with a JenOptik ProgRes CF camera attachment (c).

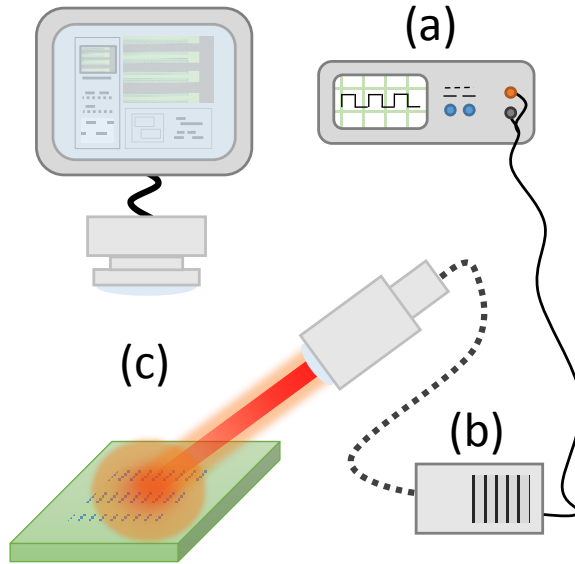


Figure 31 - Schematic of the setup used for data collection in this system.

Samples were fabricated on a single wafer, and half were coated in GNPs. Six DC levels were chosen to test the device: 0, 10, 15, 20, 25, and 30 percent. This sequence was randomized and collected from a pair of devices at each level with GNP coated and bare surfaces. Data was captured in the form of a 250 image sequence taken at ~ 3 FPS (250 images in 90 seconds). Matlab was used to process the sequences and monitor the reflection.

5.3.2 Segmenting Reflection in the Images

Image processing techniques were used to extract the reflected area and estimate the windowpane structure's radius of curvature. In Figure 32, raw images of a device's initial state is shown in (a), an intermediate heated state is in (b), and the reflection at full deflection in (c). To do the segmentation, an image is split into its RGB components, such as the (R), (G), and (B) below which are the components of (b). The pixels in the (G) component are categorized by an intensity threshold ($I > 155$) as seen in (d) in orange.

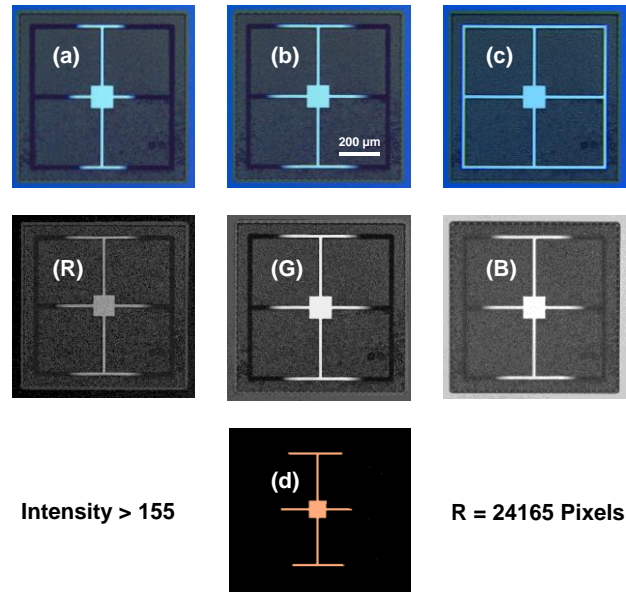


Figure 32 - Reflection profiles of a pop-up windowpane at different stages (a, b, c), with increasing temperature from left to right. The RGB components of a reflection image (R, G, and B). The segmented reflection used for a pixel count (d).

A simple pixel count is taken, and this metric is proportional to the deflection of the device, which is proportional to the light-induced temperature. This technique was applied to each sequence of 250 images at each DC and sample combination (24 total sequences). Reflectivity, as used in the following discussion, is the number of pixels with greater than the threshold intensity at a given duty cycle divided by the pixel count at room temperature for that same device.

5.4 Results

At a glance, the resulting data indicated that adding a GNP coating will improve the light absorption of the pop-up bilayer. Figure 33 shows averages of the duplicate trials of GNP-coated and bare samples at each DC over 90 seconds. The dashed lines represent bare sample averages, and solid lines have incorporated GNPs. Each color pair is at a specific DC, as labeled in the legend. As expected, higher applied power resulted in larger deflection, which is seen as a higher reflectivity in Figure 7. The Y-axis is normalized to the starting value of the zero DC trace in each averaged data set. The variation around at $t=0$ is due to variation between each device.

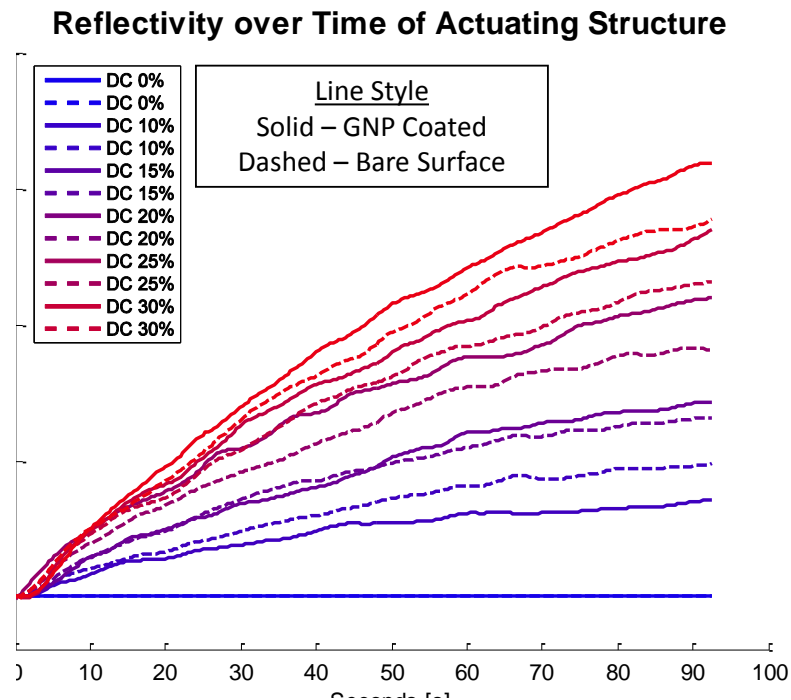


Figure 33 - Reflectivity averaged data for each sample type.

An analysis of variance (ANOVA) was performed to generate statistics on the factors present in this study, with included interactions and independent devices from set

to set. The deposition of GNPs on a device at any DC was found to be a significant factor of the resulting reflectivity ($p = 0.0042$), and therefore deflection.

5.5 Discussion

The reflectivity was taken at initial and maximum deflections for each device, and a curve was fit between the two pixel counts. Using that estimation, a conversion between reflectivity and radius of curvature has been established. The level after 90 seconds has been collected at each DC (the end points in Figure 33) and is displayed in Figure 34. This very clearly shows that there is an increased effect seen on the GNP-coated devices, shown in red.

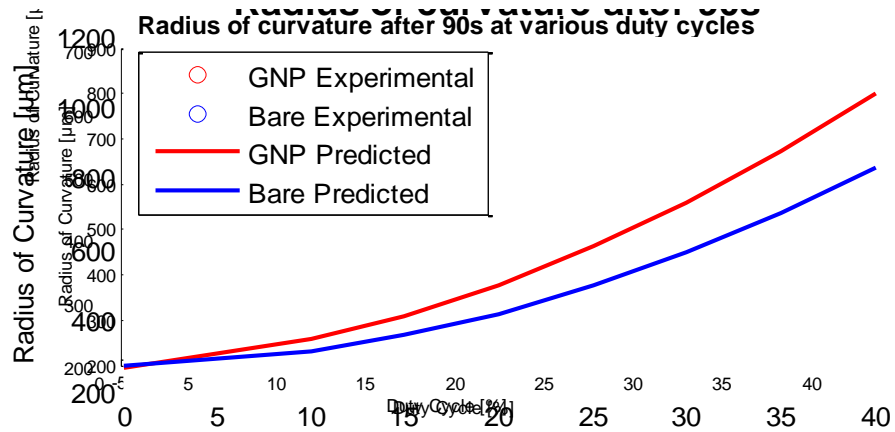


Figure 34 - Fitted curves displaying the correlation between light and deflection of the structure with error bars depicting 95% confidence interval of the fit.

The DC can be used as a direct measure of laser power being applied. The average efficiency difference can be seen by plotting the difference between the lines at each DC level, and making a linear fit. The slope of that line is 5.2, which is the percent efficiency that is added by the GNPs. Conceptually, if you make a horizontal line by +5.2% from a point on the red fit in Figure 8, it will intersect the blue fit. This is in the vicinity of previously reported efficiency calculations on a planar surface [126].

6 Conclusions from this Experiment

This work has demonstrated a hybrid of infrared absorbent gold nanoparticles and MEMS fabrication technology leading to a surface with enhanced absorption, and has potential applications in light-actuated switches and other mechanical structures. This project adds to the foundation of knowledge required for designing a system of light-powered microactuators for exploring cells' response to mechanical stimuli, and performing studies that increasing our understanding of tissue response to mechanical stresses.

CHAPTER VI

CONCLUSION

This hybrid of infrared absorbent gold nanoparticles and MEMS fabrication technology has potential applications in light-actuated switches and other mechanical structures. Deposition methods and surface chemistry are being integrated with three-dimensional MEMS structures in the next phase of this work. The long-term goal of this project is a system of light-powered microactuators for exploring cells' response to mechanical stimuli, increasing our fundamental understanding of tissue response to everyday mechanical stresses at the molecular level. To this end, there are future directions in mind that will continue the progression of this work.

6.1 Future Directions

There are multiple avenues of research that can follow the aforementioned work. The advancement can either be made with the particle film or on the MEMS structure itself. Methods for patterning multiple wavelength-specific particle films is required to integrate more complex actuation techniques, and can be accomplished in a number of ways. The MEMS structure itself can be modified per application as required by altering the geometry or materials used. Both of these routes would increase the range of functionality and usefulness of the toolset developed in this dissertation.

6.1.1 Complex and Streamlined Fabrication

Improving the absorption of a surface with single particle film is nothing more than a parlor trick, and offers no substantial improvement over a metaphorical black paint. However, the possibilities of patterning multiple wavelength-reactive regions opens interesting new opportunities. Nanoparticles tuned to different infrared wavelengths, applied at different locations on freestanding microstructures, will drive complex actuation sequences such as cyclic motions. Since the lasers were specifically chosen at wavelengths that penetrate tissue, these tiny devices could mechanically trigger cardiac cells and nerve cells through the skin without wires. As a new platform for pacemakers and for neural bypass devices, this technology could be life-changing. However, getting to that point requires better nanoparticle-patterning tools.

The foreseeable additions to the device fabrication to enhance the ability to pattern a particle film are divided into two categories. The first is to selectively apply a particle solution to the surface in a controlled dispersion technique. A second proposed method is

to universally apply the particles as previously by spin-on deposition and then remove selected regions with cleanroom-based techniques.

For patterning outside of the cleanroom, patterning can be done in a computer-controlled fashion, such as with an inkjet-like deposition or with a defined stenciling technique. These methods are both cost effective and less time consuming than including a cleanroom patterning step to the process. Stenciling would require a chemical component, where a stamp can be used to prepare a surface so when a particle solution is washed over it, the gold particles will stay on the chemically defined features.

Within cleanroom-defined patterning methods, a stenciling technique has been experimented with at the University of Louisville by etching parylene-c into a stencil after deposition on a surface, and spin-on particles are 'selected' by what passes through the stencil to the surface. The PVP component can sometimes provide troublesome linkage between wanted and unwanted regions, but stenciling avoids the problems caused by the often mischievous nature of the PVP by forcefully defining the pattern boundary.

6.1.2 IR Transparent Materials

Material changes can be made to improve the overall functionality of the structure. The largest improve could be made by changing the material so that it is less absorbent to the nIR light being used to power these devices. By building a bilayer of material that does not absorb nIR light, the difference in functionality between bare and GNP coated surfaces would be much higher. In this case, the bare would not show much heating at all, and the gold particles would drastically change the absorption profile of the surface. In theory, the efficiency difference seen between bare and nanoparticle-coated surfaces would be much higher than on reported devices.

6.2 Conclusions

This dissertation describes the successful development of a laser-driven thermal actuation method that is enhanced by the addition of gold nanoparticles. An overview of actuating MEMS was presented in chapter one to build a foundation of comparison to thermal actuation. The structural basis for the moving “pop-up” MEMS components is described in detail through the published work presented in Chapter 2. That chapter concludes that the proposed bilayer MEMS architecture is robust enough to sufficiently handle a variety of microscale tasks.

Chapter 3 introduces the motivation, theory, and methodology behind the gold nanoparticles in this work. In contrast to most other investigations of gold nanoparticles, the particle properties are examined as a surface film rather than in solution. Chapter 4 introduces the wavelength tunability of the particles as a working principle. From these two published works, it can be concluded that the thermal efficiency of a laser-driven MEMS system can be increased using gold nanoparticles, and the thermal behavior can be designed to be wavelength dependent.

Chapter 5 combines the resources investigated in the earlier chapters, and shows a resulting example of a nanoparticle-enhanced thermal actuator with large ($>100\ \mu\text{m}$) out-of-plane movement. The device is confirmed to change behavior with the deposited gold nanoparticles, and the cleanroom techniques used to successfully transfer particles from a solution to a released device are documented. This method has the potential to be developed into a more robust system for interacting with biological components. Such a system could be instrumental in facilitating mechanical stimulus at the cellular level.

REFERENCES

- [1] Jack, W.J., *Microelectromechanical systems (MEMS): fabrication, design and applications*. Smart Materials and Structures, 2001. **10**(6): p. 1115.
- [2] Hongwei, Q., F. Deyou, and X. Huikai. *A single-crystal silicon 3-axis CMOS-MEMS accelerometer*. in *Sensors, 2004. Proceedings of IEEE*. 2004.
- [3] Albarbar, A., et al., *Performance evaluation of MEMS accelerometers*. Measurement, 2009. **42**(5): p. 790-795.
- [4] Speller, K.E. and D. Yu. *A low-noise MEMS accelerometer for unattended ground sensor applications*. 2004.
- [5] Alper, S.E. and T. Akin, *A Single-Crystal Silicon Symmetrical and Decoupled MEMS Gyroscope on an Insulating Substrate*. Microelectromechanical Systems, Journal of, 2005. **14**(4): p. 707-717.
- [6] Alper, S.E., K. Azgin, and T. Akin, *A high-performance silicon-on-insulator MEMS gyroscope operating at atmospheric pressure*. Sensors and Actuators A: Physical, 2007. **135**(1): p. 34-42.
- [7] Liwei, L. and Y. Weijie. *MEMS pressure sensors for aerospace applications*. in *Aerospace Conference, 1998 IEEE*. 1998.
- [8] Palasagaram, J.N. and R. Ramadoss, *MEMS-Capacitive Pressure Sensor Fabricated Using Printed-Circuit-Processing Techniques*. Sensors Journal, IEEE, 2006. **6**(6): p. 1374-1375.

- [9] Wang, X., et al., *Diaphragm design guidelines and an optical pressure sensor based on MEMS technique*. *Microelectronics Journal*, 2006. **37**(1): p. 50-56.
- [10] Nguyen, N.T., *Micromachined flow sensors—a review*. *Flow Measurement and Instrumentation*, 1997. **8**(1): p. 7-16.
- [11] Wang, Y.-H., et al., *MEMS-based gas flow sensors*. *Microfluidics and Nanofluidics*, 2009. **6**(3): p. 333-346.
- [12] Chen, J. and L. Chang, *Development and characterization of surface micromachined, out-of-plane hot-wire anemometer*. *Microelectromechanical Systems, Journal of*, 2003. **12**(6): p. 979-988.
- [13] Adamec, R.J., D.V. Thiel, and P. Tanner. *MEMS wind direction detection: from design to operation*. in *Sensors, 2003. Proceedings of IEEE*. 2003.
- [14] Seunghyun, K., et al. *Design and fabrication of a flow sensor detecting flow direction and velocity*. in *TRANSDUCERS, Solid-State Sensors, Actuators and Microsystems, 12th International Conference on, 2003*. 2003.
- [15] Czaplewski, D.A., et al., *A micromechanical flow sensor for microfluidic applications*. *Microelectromechanical Systems, Journal of*, 2004. **13**(4): p. 576-585.
- [16] Dominique, F., et al., *An Optical MEMS-based Shear Stress Sensor for High Reynolds Number Applications*, in *41st Aerospace Sciences Meeting and Exhibit*. 2003, American Institute of Aeronautics and Astronautics.
- [17] Krijnen, G.J., et al., *MEMS based hair flow-sensors as model systems for acoustic perception studies*. *Nanotechnology*, 2006. **17**(4): p. S84-9.
- [18] Wang, Y.-H., C.-Y. Lee, and C.-M. Chiang, *A MEMS-based Air Flow Sensor with a Free-standing Micro-cantilever Structure*. *Sensors*, 2007. **7**(10): p. 2389-2401.

- [19] Du, L., Z. Zhan, and P. Cheng. *Design and Fabrication MEMS-Based Micro Solid State cantilever Wind Speed Sensor*. in *Information Acquisition, 2007. ICIA '07. International Conference on*. 2007.
- [20] Lee, C.-Y., et al., *Design and characterization of MEMS-based flow-rate and flow-direction microsensors*. *Microfluidics and Nanofluidics*, 2009. **6**(3): p. 363-371.
- [21] Berberig, O., et al. *The Prandtl micro flow sensor (PMFS): a novel silicon diaphragm capacitive sensor for flow velocity measurement*. in *Solid State Sensors and Actuators, 1997. TRANSDUCERS '97 Chicago., 1997 International Conference on*. 1997.
- [22] Bouwstra, S., et al., *Resonating microbridge mass flow sensor*. *Sensors and Actuators A: Physical*, 1990. **21**(1-3): p. 332-335.
- [23] Svedin, N., et al., *A lift-force flow sensor designed for acceleration insensitivity*. *Sensors and Actuators A: Physical*, 1998. **68**(1-3): p. 263-268.
- [24] Svedin, N., E. Kälvesten, and G. Stemme, *A lift force sensor with integrated hot-chips for wide range flow measurements*. *Sensors and Actuators A: Physical*, 2003. **109**(1-2): p. 120-130.
- [25] Buttarello, M., *Quality specification in haematology: the automated blood cell count*. *Clin Chim Acta*, 2004. **346**(1): p. 45-54.
- [26] Bentley, S.A., *Automated differential white cell counts: a critical appraisal*. *Baillieres Clin Haematol*, 1990. **3**(4): p. 851-69.
- [27] Satake, D., et al., *A sensor for blood cell counter using MEMS technology*. *Sensors and Actuators B: Chemical*, 2002. **83**(1-3): p. 77-81.
- [28] Cheung, K.C., et al., *Microfluidic impedance-based flow cytometry*. *Cytometry A*, 2010. **77**(7): p. 648-66.

- [29] Lourenco, L.M., A. Krothapalli, and C.A. Smith, *Particle Image Velocimetry*, in *Advances in Fluid Mechanics Measurements*, M. Gad-el-Hak, Editor. 1989, Springer Berlin Heidelberg. p. 127-199.
- [30] Willert, C.E. and M. Gharib, *Digital particle image velocimetry*. *Experiments in Fluids*, 1991. **10**(4): p. 181-193.
- [31] Bouaidat, S., et al., *Surface-directed capillary system; theory, experiments and applications*. *Lab Chip*, 2005. **5**(8): p. 827-36.
- [32] Nag, A., B. Panda, and A. Chattopadhyay, *Performing chemical reactions in virtual capillary of surface tension-confined microfluidic devices*. *Pramana*, 2005. **65**(4): p. 621-630.
- [33] Lam, P., K.J. Wynne, and G.E. Wnek, *Surface-Tension-Confined Microfluidics*. *Langmuir*, 2002. **18**(3): p. 948-951.
- [34] Pennisi, E., *Water's Tough Skin*. *Science*, 2014. **343**(6176): p. 1194-1197.
- [35] Koch, M., A.G.R. Evans, and A. Brunnschweiler, *Design and fabrication of a micromachined Coulter counter*. *Journal of Micromechanics and Microengineering*, 1999. **9**(2): p. 159.
- [36] Goessling, B.A., et al., *Bistable out-of-plane stress-mismatched thermally actuated bilayer devices with large deflection*. *Journal of Micromechanics and Microengineering*, 2011. **21**(6): p. 065030.
- [37] Moiseeva, E., et al., *Single-mask microfabrication of three-dimensional objects from strained bimorphs*. *Journal of Micromechanics and Microengineering*, 2007. **17**(9): p. N63.

- [38] Senousy, Y.M. and C.K. Harnett, *Fast three dimensional ac electro-osmotic pumps with nonphotolithographic electrode patterning*. *Biomicrofluidics*, 2010. **4**(3): p. -.
- [39] Chang, C.-C. and R.-J. Yang, *Electrokinetic mixing in microfluidic systems*. *Microfluidics and Nanofluidics*, 2007. **3**(5): p. 501-525.
- [40] Jacobson, S.C., T.E. McKnight, and J.M. Ramsey, *Microfluidic Devices for Electrokinetically Driven Parallel and Serial Mixing*. *Analytical Chemistry*, 1999. **71**(20): p. 4455-4459.
- [41] Pethig, R. and G.H. Markx, *Applications of dielectrophoresis in biotechnology*. *Trends in Biotechnology*, 1997. **15**(10): p. 426-432.
- [42] Lennart, L. and G.-e.-H. Mohamed, *MEMS-based pressure and shear stress sensors for turbulent flows*. *Measurement Science and Technology*, 1999. **10**(8): p. 665.
- [43] Yi-Kuen, L., et al. *Chaotic mixing in electrokinetically and pressure driven micro flows*. in *Micro Electro Mechanical Systems, 2001. MEMS 2001. The 14th IEEE International Conference on*. 2001.
- [44] Yang, Z., et al., *Ultrasonic micromixer for microfluidic systems*. *Sensors and Actuators A: Physical*, 2001. **93**(3): p. 266-272.
- [45] Yaralioglu, G.G., et al., *Ultrasonic Mixing in Microfluidic Channels Using Integrated Transducers*. *Analytical Chemistry*, 2004. **76**(13): p. 3694-3698.
- [46] Tsai, J.-H. and L. Lin, *Active microfluidic mixer and gas bubble filter driven by thermal bubble micropump*. *Sensors and Actuators A: Physical*, 2002. **97-98**(0): p. 665-671.
- [47] Nicholas, J.C., J.T. Zachary, and K. Sang-Gook, *A strain amplifying piezoelectric MEMS actuator*. *Journal of Micromechanics and Microengineering*, 2007. **17**(4): p. 781.

- [48] Tadigadapa, S. and K. Mateti, *Piezoelectric MEMS sensors: state-of-the-art and perspectives*. Measurement Science and Technology, 2009. **20**(9): p. 092001.
- [49] Bütetfisch, S., V. Seidemann, and S. Büttgenbach, *Novel micro-pneumatic actuator for MEMS*. Sensors and Actuators A: Physical, 2002. **97–98**(0): p. 638-645.
- [50] Wagner, B., et al. *Bistable microvalve with pneumatically coupled membranes*. in *Micro Electro Mechanical Systems, 1996, MEMS '96, Proceedings. An Investigation of Micro Structures, Sensors, Actuators, Machines and Systems. IEEE, The Ninth Annual International Workshop on*. 1996.
- [51] Xing, Y., et al. *A MEMS thermopneumatic silicone membrane valve*. in *Micro Electro Mechanical Systems, 1997. MEMS '97, Proceedings, IEEE., Tenth Annual International Workshop on*. 1997.
- [52] Takao, H., et al., *A MEMS microvalve with PDMS diaphragm and two-chamber configuration of thermo-pneumatic actuator for integrated blood test system on silicon*. Sensors and Actuators A: Physical, 2005. **119**(2): p. 468-475.
- [53] Lendlein, A. and R. Langer, *Biodegradable, Elastic Shape-Memory Polymers for Potential Biomedical Applications*. Science, 2002. **296**(5573): p. 1673-1676.
- [54] Wolf, R.H. and A.H. Heuer, *TiNi (shape memory) films silicon for MEMS applications*. Microelectromechanical Systems, Journal of, 1995. **4**(4): p. 206-212.
- [55] Berger, J.D., et al. *Widely tunable external cavity diode laser based on a MEMS electrostatic rotary actuator*. in *Optical Fiber Communication Conference and Exhibit, 2001. OFC 2001*. 2001.

- [56] Chia-Hua, C., et al., *A low actuation voltage electrostatic actuator for RF MEMS switch applications*. Journal of Micromechanics and Microengineering, 2007. **17**(8): p. 1649.
- [57] Desai, A., S.-W. Lee, and Y.-C. Tai, *A MEMS electrostatic particle transportation system*. Sensors and Actuators A: Physical, 1999. **73**(1–2): p. 37-44.
- [58] Chia-Yen, L., C. Hsien-Tsung, and W. Chih-Yung, *A MEMS-based valveless impedance pump utilizing electromagnetic actuation*. Journal of Micromechanics and Microengineering, 2008. **18**(3): p. 035044.
- [59] Chowdhury, S., et al. *A modular MEMS electromagnetic actuator for use in a hearing instrument*. in *Circuits and Systems, 2000. Proceedings of the 43rd IEEE Midwest Symposium on*. 2000.
- [60] Klintberg, L., et al., *A large stroke, high force paraffin phase transition actuator*. Sensors and Actuators A: Physical, 2002. **96**(2–3): p. 189-195.
- [61] Hantschel, T. and E.M. Chow, *S-shaped double-spring structures for high stiffness and spring height*. Microelectronic Engineering, 2012. **97**(0): p. 231-234.
- [62] Liu, K., et al., *Powerful, Multifunctional Torsional Micromuscles Activated by Phase Transition*. Advanced Materials, 2013: p. n/a-n/a.
- [63] lab, J.s.N.E.a.A.A.N.T., *Comparison of EAPs with Other Actuator Technologies*.
- [64] Slava, K., et al., *The pull-in behavior of electrostatically actuated bistable microstructures*. Journal of Micromechanics and Microengineering, 2008. **18**(5): p. 055026.

- [65] Yao-Joe, Y., L. Bo-Ting, and K. Wen-Cheng, *A novel 2×2 MEMS optical switch using the split cross-bar design*. Journal of Micromechanics and Microengineering, 2007. **17**(5): p. 875.
- [66] Yibo, W., Z. Congchun, and D. Guifu. *Vertically bidirectional bistable microrelay with magnetostatic and thermal actuations*. in *Micro Electro Mechanical Systems (MEMS), 2010 IEEE 23rd International Conference on*. 2010.
- [67] Luharuka, R. and P.J. Hesketh, *Design of fully compliant, in-plane rotary, bistable micromechanisms for MEMS applications*. Sensors and Actuators A: Physical, 2007. **134**(1): p. 231-238.
- [68] Usha, R.G., M.W. Kevin, and A.B. Thomas, *Fabrication of polyimide bi-stable diaphragms using oxide compressive stresses for the field of 'Buckle MEMS'*. Journal of Micromechanics and Microengineering, 2010. **20**(7): p. 075013.
- [69] Receveur, R.A.M., et al. *Laterally moving bi-stable MEMS DC-switch for biomedical applications*. in *Micro Electro Mechanical Systems, 2004. 17th IEEE International Conference on. (MEMS)*. 2004.
- [70] Kuekes, P.J., D.R. Stewart, and R.S. Williams, *The crossbar latch: Logic value storage, restoration, and inversion in crossbar circuits*. Journal of Applied Physics, 2005. **97**(3): p. 034301-034301-5.
- [71] Hoffmann, M., P. Kopka, and E. Voges, *All-silicon bistable micromechanical fiber switch based on advanced bulk micromachining*. Selected Topics in Quantum Electronics, IEEE Journal of, 1999. **5**(1): p. 46-51.

- [72] Qiu, J., J.H. Lang, and A.H. Slocum. *A centrally-clamped parallel-beam bistable MEMS mechanism*. in *Micro Electro Mechanical Systems, 2001. MEMS 2001. The 14th IEEE International Conference on*. 2001.
- [73] Charlot, B., et al., *Bistable nanowire for micromechanical memory*. *Journal of Micromechanics and Microengineering*, 2008. **18**(4): p. 045005.
- [74] Park, S. and D. Hah, *Pre-shaped buckled-beam actuators: Theory and experiments*. *Sensors and Actuators A: Physical*, 2008. **148**(1): p. 186-192.
- [75] Vangbo, M., *An analytical analysis of a compressed bistable buckled beam*. *Sensors and Actuators A: Physical*, 1998. **69**(3): p. 212-216.
- [76] Koch, K., H.F. Bohn, and W. Barthlott, *Hierarchically sculptured plant surfaces and superhydrophobicity*. *Langmuir*, 2009. **25**(24): p. 14116-20.
- [77] Konrad, W., et al., *Applying Methods from Differential Geometry to Devise Stable and Persistent Air Layers Attached to Objects Immersed in Water*. *Journal of Bionic Engineering*, 2009. **6**(4): p. 350-356.
- [78] Chen, C.C., J.S. Wang, and O. Solgaard, *Micromachined bubble-jet cell sorter with multiple operation modes*. *Sensors and Actuators B: Chemical*, 2006. **117**(2): p. 523-529.
- [79] Chen, P.-H., et al., *Droplet formation of a thermal sideshooter inkjet printhead*. *International Journal of Heat and Fluid Flow*, 1998. **19**(4): p. 382-390.
- [80] Prakash, M. and N. Gershenfeld, *Microfluidic Bubble Logic*. *Science*, 2007. **315**(5813): p. 832-835.
- [81] Kohnle, J., et al. *A unique solution for preventing clogging of flow channels by gas bubbles*. in *Micro Electro Mechanical Systems, 2002. The Fifteenth IEEE International Conference on*. 2002.

- [82] Hallberg, F., et al., *Sensitive and robust electrophoretic NMR: Instrumentation and experiments*. Journal of Magnetic Resonance, 2008. **192**(1): p. 69-77.
- [83] Yan, D., et al., *Biofilm structure and its influence on clogging in drip irrigation emitters distributing reclaimed wastewater*. Journal of Environmental Sciences, 2009. **21**(6): p. 834-841.
- [84] Nørskov, J.K., et al., *Origin of the Overpotential for Oxygen Reduction at a Fuel-Cell Cathode*. The Journal of Physical Chemistry B, 2004. **108**(46): p. 17886-17892.
- [85] Silva, P.R.M., et al., *Development of Hg-electroplated-iridium based microelectrode arrays for heavy metal traces analysis*. Analytica Chimica Acta, 1999. **385**(1-3): p. 249-255.
- [86] Xie, X., et al., *Development of an ultramicroelectrode arrays (UMEAs) sensor for trace heavy metal measurement in water*. Sensors and Actuators B: Chemical, 2004. **97**(2-3): p. 168-173.
- [87] Harnett, C.K., et al. *Microscopic containers for sample archiving in environmental and biomedical sensors*. in *Instrumentation and Measurement Technology Conference (I2MTC), 2010 IEEE*. 2010.
- [88] Onda, K., et al., *Prediction of production power for high-pressure hydrogen by high-pressure water electrolysis*. Journal of Power Sources, 2004. **132**(1-2): p. 64-70.
- [89] Nagai, N., M. Takeuchi, and M. Nakao, *Effects of Generated Bubbles Between Electrodes on Efficiency of Alkaline Water Electrolysis*. JSME International Journal Series B Fluids and Thermal Engineering, 2003. **46**(4): p. 549-556.
- [90] Yang, J., et al., *Very Small Bubble Formation at the Solid-Water Interface*. The Journal of Physical Chemistry B, 2003. **107**(25): p. 6139-6147.

- [91] Py, C., et al., *Capillary Origami: Spontaneous Wrapping of a Droplet with an Elastic Sheet*. Physical Review Letters, 2007. **98**(15): p. 156103.
- [92] Tucker, A.S. and C.A. Ward, *Critical state of bubbles in liquid‐gas solutions*. Journal of Applied Physics, 1975. **46**(11): p. 4801-4808.
- [93] Lucas, T.M. and C.K. Harnett, *Control of electrolysis-generated microbubbles for sensor surface passivation*. Applied Physics Letters, 2011. **98**(1): p. 011915-011915-3.
- [94] Roodenburg, D., et al., *Buckling beam micromechanical memory with on-chip readout*. Applied Physics Letters, 2009. **94**(18): p. 183501-183501-3.
- [95] Miller, R.A., et al. *An electromagnetic MEMS 2×2 fiber optic bypass switch*. in *Solid State Sensors and Actuators, 1997. TRANSDUCERS '97 Chicago., 1997 International Conference on*. 1997.
- [96] Tze-Wei, Y., K.L.E. Law, and A. Goldenberg, *MEMS optical switches*. Communications Magazine, IEEE, 2001. **39**(11): p. 158-163.
- [97] Zhou, J., et al., *Optically interrogated MEMS pressure sensors for propulsion applications*. Optical Engineering, 2001. **40**(4): p. 598-604.
- [98] Ohnstein, T., et al. *Micromachined silicon microvalve*. in *Micro Electro Mechanical Systems, 1990. Proceedings, An Investigation of Micro Structures, Sensors, Actuators, Machines and Robots. IEEE*. 1990. IEEE.
- [99] Jericho, S.K., et al., *Micro-electro-mechanical systems microtweezers for the manipulation of bacteria and small particles*. Review of Scientific Instruments, 2004. **75**(5): p. 1280-1282.

- [100] Eells, J.T., et al., *Mitochondrial signal transduction in accelerated wound and retinal healing by near-infrared light therapy*. *Mitochondrion*, 2004. **4**(5–6): p. 559-567.
- [101] Gobin, A.M., et al., *Near-Infrared Resonant Nanoshells for Combined Optical Imaging and Photothermal Cancer Therapy*. *Nano Letters*, 2007. **7**(7): p. 1929-1934.
- [102] Sinclair, M.J. *A high force low area MEMS thermal actuator*. in *Thermal and Thermomechanical Phenomena in Electronic Systems, 2000. IThERM 2000. The Seventh Intersociety Conference on*. 2000.
- [103] Lang, W., K. Kuhl, and H. Sandmaier. *Absorbing layers for thermal infrared detectors*. in *Solid-State Sensors and Actuators, 1991. Digest of Technical Papers, TRANSDUCERS '91., 1991 International Conference on*. 1991.
- [104] Liu, Y., et al., *Self-folding of polymer sheets using local light absorption*. *Soft Matter*, 2012. **8**(6): p. 1764-1769.
- [105] Rogalski, A., *Infrared detectors: an overview*. *Infrared Physics & Technology*, 2002. **43**(3–5): p. 187-210.
- [106] Grubisha, D.S., et al., *Femtomolar Detection of Prostate-Specific Antigen: An Immunoassay Based on Surface-Enhanced Raman Scattering and Immunogold Labels*. *Analytical Chemistry*, 2003. **75**(21): p. 5936-5943.
- [107] Hirsch, L.R., et al., *A Whole Blood Immunoassay Using Gold Nanoshells*. *Analytical Chemistry*, 2003. **75**(10): p. 2377-2381.
- [108] Niidome, T., et al., *PEG-modified gold nanorods with a stealth character for in vivo applications*. *Journal of Controlled Release*, 2006. **114**(3): p. 343-347.

- [109] Talghader, J.J., A.S. Gawarikar, and R.P. Shea, *Spectral selectivity in infrared thermal detection*. *Light Sci Appl*, 2012. **1**: p. e24.
- [110] Alric, C., et al., *Gadolinium Chelate Coated Gold Nanoparticles As Contrast Agents for Both X-ray Computed Tomography and Magnetic Resonance Imaging*. *Journal of the American Chemical Society*, 2008. **130**(18): p. 5908-5915.
- [111] Eustis, S. and M.A. El-Sayed, *Why gold nanoparticles are more precious than pretty gold: Noble metal surface plasmon resonance and its enhancement of the radiative and nonradiative properties of nanocrystals of different shapes*. *Chemical Society Reviews*, 2006. **35**(3): p. 209-217.
- [112] Baffou, G., R. Quidant, and F.J. García de Abajo, *Nanoscale Control of Optical Heating in Complex Plasmonic Systems*. *ACS Nano*, 2010. **4**(2): p. 709-716.
- [113] Zhang, G., et al., *Tunability and stability of gold nanoparticles obtained from chloroauric acid and sodium thiosulfate reaction*. *Nanoscale Research Letters*, 2012. **7**(1): p. 337.
- [114] Huang, X., et al., *Cancer Cell Imaging and Photothermal Therapy in the Near-Infrared Region by Using Gold Nanorods*. *Journal of the American Chemical Society*, 2006. **128**(6): p. 2115-2120.
- [115] Zheng, M., et al., *Optical properties of silver-dispersed PVP thin film*. *Materials Research Bulletin*, 2001. **36**(5–6): p. 853-859.
- [116] Baffou, G. and R. Quidant, *Thermo-plasmonics: using metallic nanostructures as nano-sources of heat*. *Laser & Photonics Reviews*, 2013. **7**(2): p. 171-187.

- [117] Reynolds, F.W., *Some Effects of Gas upon the Resistance and Resistance-Temperature Coefficient of Sputtered Platinum Films*. Physical Review, 1924. **24**(5): p. 523-531.
- [118] Koller, L.R., *Physical Properties of Thin Metallic Films. III. Some Factors Affecting the Resistance of Sputtered Platinum Films*. Physical Review, 1921. **18**(3): p. 221-235.
- [119] Ilic, B. and H.G. Craighead, *Topographical Patterning of Chemically Sensitive Biological Materials Using a Polymer-Based Dry Lift Off*. Biomedical Microdevices, 2000. **2**(4): p. 317-322.
- [120] Selvarasah, S., et al., *A reusable high aspect ratio parylene-C shadow mask technology for diverse micropatterning applications*. Sensors and Actuators A: Physical, 2008. **145–146**(0): p. 306-315.
- [121] Chronis, N. and L.P. Lee, *Electrothermally Activated SU-8 Microgripper for Single Cell Manipulation in Solution*. Microelectromechanical Systems, Journal of, 2005. **14**(4): p. 857-863.
- [122] Keekyoung, K., et al., *Nanonewton force-controlled manipulation of biological cells using a monolithic MEMS microgripper with two-axis force feedback*. Journal of Micromechanics and Microengineering, 2008. **18**(5): p. 055013.
- [123] Que, L., J.S. Park, and Y.B. Gianchandani. *Bent-beam electro-thermal actuators for high force applications*. in *Micro Electro Mechanical Systems, 1999. MEMS '99. Twelfth IEEE International Conference on*. 1999.

- [124] Comtois, J.H. and V.M. Bright. *Surface micromachined polysilicon thermal actuator arrays and applications*. in *Proc. Solid-State Sensor and Actuator Workshop*. 1996.
- [125] James, K., et al., *Effect of Molecular Weight Cut-off of Cellulose Membranes on High Yield Production of Gold/Gold Sulfide Nanoparticles*.
- [126] Lucas, T.M., et al., *Thermal properties of infrared absorbent gold nanoparticle coatings for MEMS applications*. *Sensors and Actuators A: Physical*, 2013. **198**(0): p. 81-86.
- [127] Jain, P.K., W. Huang, and M.A. El-Sayed, *On the Universal Scaling Behavior of the Distance Decay of Plasmon Coupling in Metal Nanoparticle Pairs: A Plasmon Ruler Equation*. *Nano Letters*, 2007. **7**(7): p. 2080-2088.
- [128] Huang, D., et al., *Plastic-Compatible Low Resistance Printable Gold Nanoparticle Conductors for Flexible Electronics*. *Journal of The Electrochemical Society*, 2003. **150**(7): p. G412-G417.
- [129] Oldenburg, S.J., et al., *Nanoengineering of optical resonances*. *Chemical Physics Letters*, 1998. **288**(2-4): p. 243-247.
- [130] Chen, H., et al., *Gold nanorods and their plasmonic properties*. *Chemical Society Reviews*, 2013. **42**(7): p. 2679-2724.
- [131] O'Neal, D.P., et al., *Photo-thermal tumor ablation in mice using near infrared-absorbing nanoparticles*. *Cancer Letters*, 2004. **209**(2): p. 171-176.
- [132] Hirsch, L.R., et al., *Nanoshell-mediated near-infrared thermal therapy of tumors under magnetic resonance guidance*. *Proceedings of the National Academy of Sciences*, 2003. **100**(23): p. 13549-13554.

[133] Lucas, T.M., et al., *Wavelength specific excitation of gold nanoparticle thin-films*. Applied Physics Letters, 2014. **104**(1): p. 011909 - 011909.

CURRICULUM VITAE

1104 Poplar Level Plaza #18, Louisville KY, 40217

Phone: 606-571-1081

Email: tmluca01@louisville.edu

Summary

Available: August 2014

- Areas of focus in graduate career:
 - Microelectromechanical Systems (MEMS) Design
 - Microfluidics Applications
- EIT Certification: **Passed** FE Exam, EIT No. 13905
- Experienced with working in teams to accomplish objectives
- Trained in many MEMS fabrication techniques including: Lithography, Thin-film Deposition, Thermal Processing, Wet and Dry Etching, Metrology and Testing, SEM Imaging
- Software proficiency: Matlab, L-Edit, Coventorware, Silvaco (Athena, Atlas), LabVIEW, Rockwell RSLogix 500/5000, Microsoft Office Products

Education

Ph.D. in in Electrical and Computer Engineering

University of Louisville, Speed School of Engineering, Louisville, KY May 2014

Focus: Novel functionality of hybrid MEMS/nanoparticle structures

M.Eng. Degree in Electrical and Computer Engineering

University of Louisville, Speed School of Engineering, Louisville, KY August
2010

Thesis Topic: Microbubble Generation and Control

B.S. Degree in Electrical and Computer Engineering

University of Louisville, Speed School of Engineering, Louisville, KY August
2009

Publications

Lucas, T. M., James, K. T., Beharic, J., Moiseeva, E. V., O'Toole, M. G., Harnett, C. K., "Wavelength specific excitation of gold nanoparticle thin-films", Appl. Phys. Lett. 104 (2014)

Lucas, T. M., Moiseeva, E. V., Zhang, G., Gobin, A. M., Harnett, C. K., "Thermal properties of infrared absorbent gold nanoparticle coatings for MEMS applications", Sensors and Actuators A: Physical, Volume 198, 15 August 2013, Pages 81-86

Goessling, B. A., **Lucas, T. M.**, Aebersold, J. W., Moiseeva E. V., Harnett, C. K., "Bistable Out-of-Plane Stress Mismatched Thermally Actuated Bilayer Devices with Large Deflection", J. Micromech. Microeng. 21 (2011)

Lucas, T. M., Harnett, C. K., "Control of electrolysis-generated microbubbles for sensor surface passivation", Appl. Phys. Lett. 98 (2011)

Conference Presentations

Thomas Lucas, Evgeniya Moiseeva, Cindy Harnett, "Progress Towards a Light-Driven Bistable Microactuator", KIEC 2013 Conference, Lexington KY, August 2013 *Poster*

Jasmin Beharic, Yehya M. Senousy, **Thomas M. Lucas**, Cindy K. Harnett, "Flexible Sensors for Shape Detection", KY NanoSymposium 2013, University of Louisville, Kentucky, August 16-17 2013 *Poster*

T. M. Lucas, J. Beharic, Y. M. Senousy, E. V. Moiseeva, C. K. Harnett, "Characterization of a Bistable Microstructure for Bidirectional Air Flow Threshold Sensing", KY NanoSymposium 2013, University of Louisville, Kentucky, August 16-17 2013 *Presentation*

Thomas Lucas, Evgeniya Moiseeva, Cindy Harnett, "Thermal Properties of Infrared Absorbent Gold Nanoparticle Coatings", The 7th Int. Conference of Microtechnologies in Medicine and Biology, Marina Del Ray CA, April 2013 *Presentation and Poster*

Thomas Lucas, Evgeniya Moiseeva, Guandong Zhang, Andre Gobin, Cindy Harnett, "Design and Simulation of Optically Actuated Bistable MEMS", 8th KIEC 2012 Conference, Louisville KY, June 2012 *Poster*

Evgeniya Moiseeva, **Thomas Lucas**, Guandong Zhang, Andre Gobin, Cindy Harnett, "Development of a MEMS Bistable Actuator Incorporated with Nanoparticles", 17th Annual KY EPSCoR Conference, Lexington KY, May 2012

Poster

Evgeniya Moiseeva, **Thomas Lucas**, Guandong Zhang, Andre Gobin, Cindy Harnett, "Light-Powered Nanoparticle-MEMS Hybrid", American Physical Society March Meeting, Boston MA, March 2012

Presentation

Thomas Lucas, Evgeniya Moiseeva, Cindy Harnett, "Design and Simulation of Optically Actuated Bistable MEMS", American Physical Society March Meeting, Boston MA, March 2012

Poster

Lucas, T. M., Harnett, C. K., "A Low-Cost Conductivity Sensor with Data Logging", 16th Annual KY EPSCoR Conference, Louisville KY, May 2011

Poster

Harnett, C. K., **Lucas, T. M.**, Aebersold, J. W, "Interaction of thin-film microcoils with the air/water interface and applications in microfluidics", Presentation at American Physical Society Meeting, Portland OR, March 17, 2010

Presentation